Development of Femtosecond Laser Desorption/Ionization Time-of-Flight Mass Spectrometer based on Ion Trajectory Simulation

Jianzhong Wang

Department of Physics, Graduate School of Science,

Osaka University

March, 2023

TABLE OF CONTENTS

1 Introduction

Since 1985, the laser desorption/ionization technique was first introduced for pulsed ion source generation in time-of-flight (TOF) mass spectrometry (MS), matrix-assisted laser desorption/ionization mass spectrometry (MALDI-MS) [1] has evolved rapidly as a routine analytical tool. In the same year, chirped pulse amplification (CPA) [2] technique was also invented, and ultrafast optics came to the horizon, but the application of femtosecond laser was not widespread yet in mass spectrometry, the majority of the lasers used for desorption/ionization were still nanosecond lasers. For the laser desorption/ionization TOF mass spectrometer optimization, mass resolution R as the criterion for mass spectrometer performance can be expressed as

$$R = \frac{T}{2\Delta t} \approx \frac{\Delta v}{v}, \tag{1.1}$$

where T is the total flight time of the ion in the system, Δt is the full width at half maximum of the peak in a TOF spectrum, velocity v and velocity difference Δv, and the total flight time is inverse to the velocity because of the same flight length. The energy spread of laser-desorbed ions always causes a bad effect on R because of the initial ion velocity distribution. With the femtosecond laser technique gradually matured, laser-produced plasmas by using ultrafast laser pulses have been widely used for high-precision industrial manufacturing and applied to plume hydrodynamics research. Analytical applications also have laser-induced breakdown spectroscopy (LIBS), and laser-ablation inductively coupled plasma mass spectrometry (LA-ICP-MS) in biomaterials. Still, most research is based on high-intensity laser ablation and a large number of sample particles dissociate. Verhoff [3] and Freeman [4] by comparing femtosecond and nanosecond laser-induced ions found that the femtosecond laser-desorbed ions have a narrower angular distribution which is more suitable for R improvement. At the same time, the intensity of a femtosecond laser also affects the energy distribution of the ions. For lasers with different pulse durations and intensities, the velocity distribution is shown in **Figure1.1**; the left side shows the schematic diagram of the interaction between the laser pulse and the sample surface, and the right side shows the corresponding ion velocity distribution and energy level.
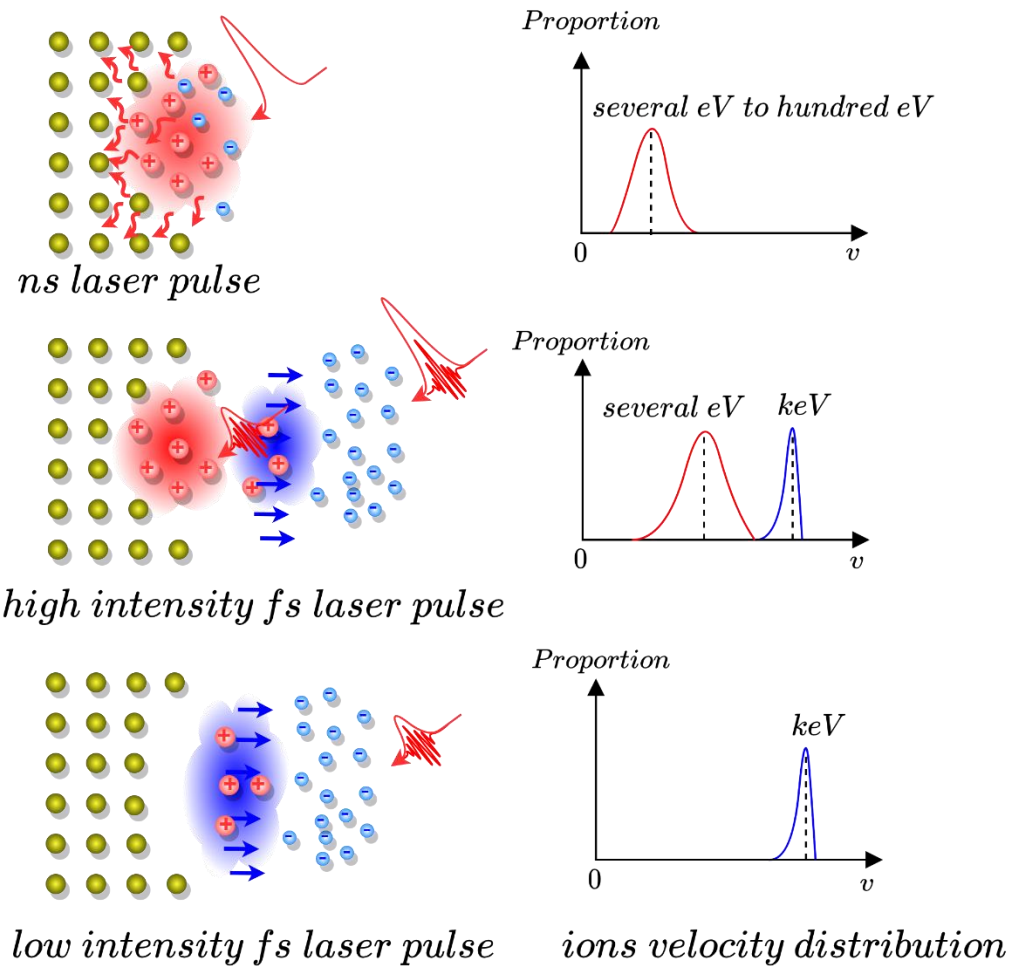
3

Figure 1.1 –Schematic diagram of the interaction between the
laser pulse and the sample surface

In the **Figure1.1** nanosecond laser pulse case, the pulse duration is long enough for energy transfer between ions and lattice, the lattice absorbs part of the pulse energy, and the ion bunch reaches thermal equilibrium. The kinetic energy distribution of the ions ranges from eV to several hundred eV depending on the intensity of the nanosecond laser. In the high intensity femtosecond laser pulse case illustrated in **Figure 1.1** center graph, part of the energy from the short powerful pulse will elevate the electron energy during the pulse duration and enable energetic electrons to escape from the sample surface. The escaped electrons create a strong electrostatic field of charge separation, which drags a small number of ions from the sample surface [5]. The ions emitted at this stage

correspond to the blue ion cloud and the blue curve in the kinetic energy distribution of ion of keV. Extra pulse energy will be used to increase the energy and collisions among electrons and ions, and a large number of ions will emit. This stage corresponds to the red ion cloud and the red curve with energy of several eV. By reducing the pulse intensity as illustrated in **Figure1.1** bottom graph of low intensity femtosecond laser pulse case, if the energy of the pulse is only used for electrons and no additional energy for the lattice and ions, the desorption/ionization of a small number of samples with high-velocity emission may be achieved. Therefore, in order to explore this emission process, and improve the mass resolution R by figuring out the relationship between Δv and v, in this study a TOF mass spectrometer combined with femtosecond laser was employed. Depending on the ions emission simulation and the trajectory simulation in the system, the detected ion TOF spectra can be analyzed profoundly to observe the ions velocity distribution and to further understand the fundamental mechanism of low-intensity femtosecond laser desorption/ionization.

1.1 Time-of-flight (TOF) mass spectrometer

When the system of time-of-flight (TOF) mass spectrometer was invented by W. E. Stephens [6] in 1946, the ions having different mass-to-charge ratio m/z are dispersed in time in an equal field-free drift path to distinguish ion charge state and species, and TOF mass spectrometer becomes the most classical type in mass spectrometer history. A scheme of a linear TOF mass spectrometer setup is shown in **Figure 1.2**.
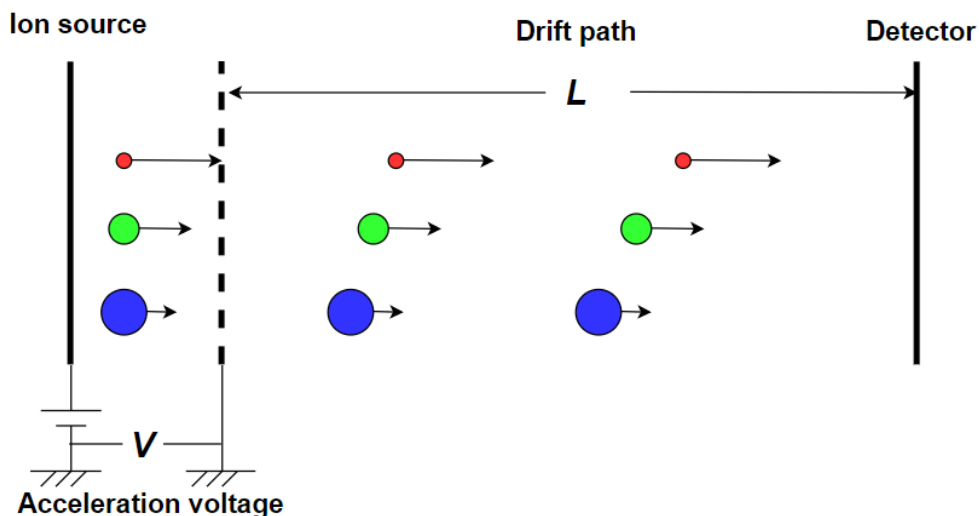

Figure 1.2 – Scheme of the set-up of a linear TOF mass spectrometer

In terms of a TOF mass spectrometer as a portable and easy-to-assemble mass spectrometer, the initial velocity and position of ions are usually unevenly distributed caused by the ionization method and process. Therefore, for the TOF mass spectrometer system, the subsequent development and optimization methods are increasing the drift path length or using delay extraction method [7]. In that case, the most commonly used mass spectrometers are reflector time-of-flight mass spectrometer [8] and two-stage acceleration [9] mass spectrometer. For increasing flight paths, the MULTUM Linear plus TOF anlyzer [10] effectively elongated the flight paths within a compact structure and realized high performance.

1.2 Femtosecond interaction with matter mechanisms

The interaction of ultrashort laser pulse approximate time scales of nanosecond and femtosecond energy absorption with different materials involves various phenomena and

mechanisms within and after the laser pulse. In general, the laser interaction with matter can be divided into thermal and non-thermal according to pulse duration time scale and pulse energy [11] [12], as shown in **Figure 1.3**, because the energy relaxation process will occur between electron and lattice in metal when the pulse duration is 1~10 picosecond (ps) or longer. Therefore, the pulse duration is shorter than the picosecond level can achieve the sample ionization without heat transfer to the lattice and call it non-thermal. For the nanosecond laser, the laser pulse energy transfer to the lattice and electron dramatically, and the relationship between various ionizations and the pulse widths corresponding to those reactions [13] [14] are shown in **Figure 1.4**. Reasonable laser pulse duration and intensity can realize the desorption/ionization of the sample without destroying the surface.
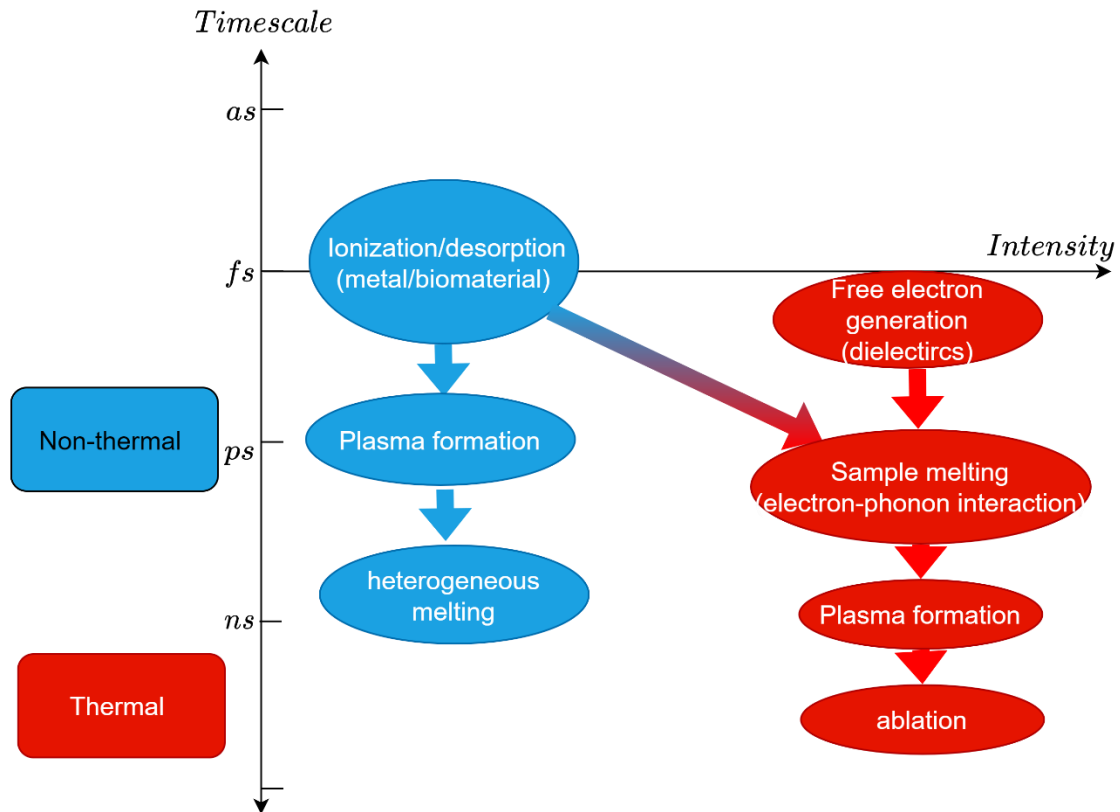
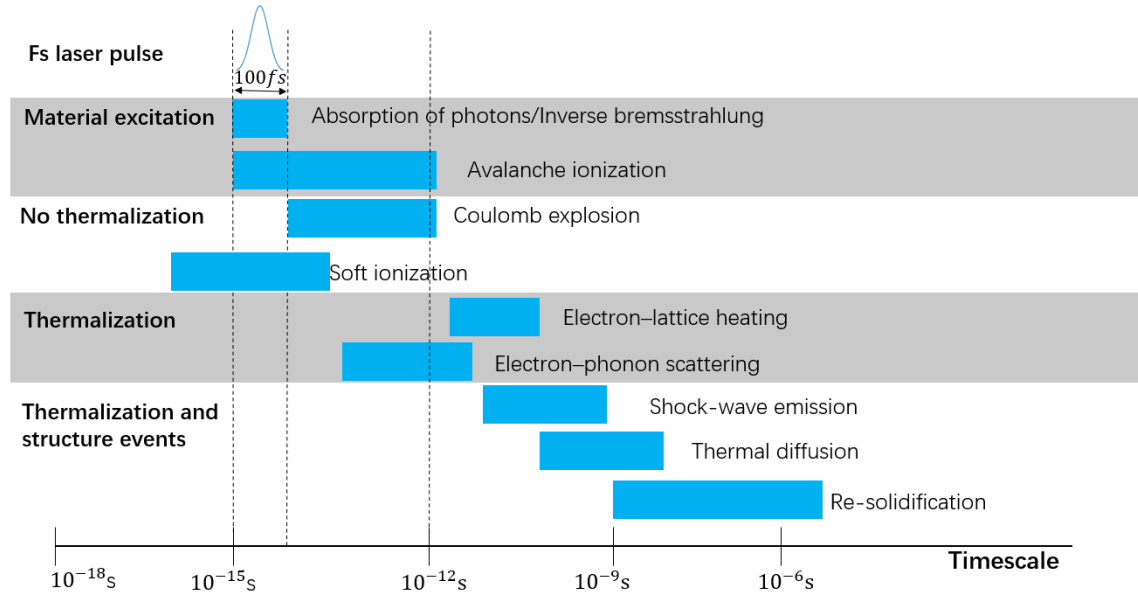Figure 1.3 – Laser interaction mechanism under time scales

Figure 1.4 –Relationship between various ionizations and the pulse widths corresponding to those reactions

1.3 Femtosecond laser-induced plasma velocity distribution

Laser-produced plasmas by using ultrafast laser pulses have been widely used for plume hydrodynamics research. The initial velocity distribution of ions can be observed using ultrafast laser ionization, through the combination with the TOF mass spectrometer and effective use of an acceleration electrostatic lens system. Kools et al. [15] use angular resolved TOF spectra combined with Maxwell-Boltzmann (MB) distribution model to analyze and fit the initial velocity distribution of the Cu ion using $(28ns, \lambda = 308nm; 90mJ\ per\ pulse)$ laser ablation deposition, and proposed a shift term for the MB distribution by adding the plasma stream velocity which is normal to the target. Ye [16] also used Ti: sapphire laser pulse (80 femtosecond full width at half maximum at 800 nm) to ionize metal titanium combined with the reflector TOF mass spectrometer, achieved kinetic energy observation and the fast ions range from 3 to 10 keV, and experiment data fitted well by using shifted MB distribution with shift term of plasma stream velocity. Regarding the laser matter interaction with different laser intensities and pulse duration, Verhoff et al .[3] investigated the angular distribution of ions and atoms showed femtosecond laser-induced narrower angular distribution and broader energy distribution comparing with nanosecond laser. Freeman et al.[4] used intensified charge-

8

coupled device (ICCD) to observe the plasma expansion induced by femtosecond laser and nanosecond laser separately. Their results are reprinted in **Figure 1.5**.
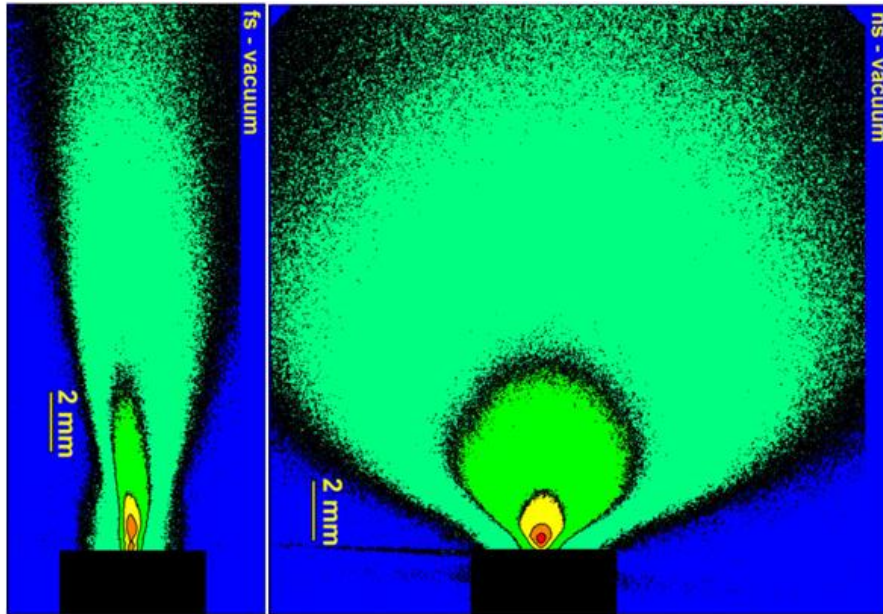
Figure 1.5 –ICCD image of plasma expansion with different pulse widths.
Reprinted from [4]

Torrisi et al. found that with the 9 ns wavelength 1064nm 1-900mJ pulse energy laser, the tantalum ions energy distribution is presented as a function of the charge states [17]. Therefore, they proposed the new velocity shift term of the Coulomb velocity term in the original shifted MB distribution, which was affected by the ion charge state. Other group [18] also conducted a similar experiment to testify the Coulomb velocity term effect by using the aluminum ions with different charge states under nanosecond laser.

Purpose

As mentioned earlier, to explore the low-intensity femtosecond laser desorption/ionization process, and to expect to desorb and ionize with fast emission in a small number of samples, a further detailed understanding of the basic mechanism is needed. This understanding is also expected to be a stepping stone toward improving the resolution (suppress the energy distribution of emitted ions) of mass spectrometry. In order to understand the basic mechanism, it is necessary to obtain and evaluate the initial velocity distribution of ions.

2 Instrumentation

INTRODUCTION

The experimental system is introduced in this chapter. The practical system is divided into the light source system and the TOF mass spectrometer. The light source system consists of a femtosecond (fs) pulsed laser and an optical path. This optical path is used to femtosecond laser pulse shaping, including the intensity, the pulse duration, and the final sample ionization position. The TOF mass spectrometer consists of an ion source housing, an electric acceleration field, a drift tube, and a detector.

2.1 Femtosecond laser system

This section introduced the laser source and the optical path section for pulse generating and shaping.

2.1.1 Laser source

The laser source: The laser used in these experiments is a Coherent Ti: sapphire femtosecond laser system. The Rega 9000 amplifier is seeded with the Mira 900 mode-locked oscillator and pumped by the Verdi-V18 Nd: YVO_4 laser. The Verdi-V18 also pumps the Mira 900 femtosecond oscillator. The regenerative amplifier produces pulses of linearly polarized light at 800 nm with a 10 kHz repetition rate.
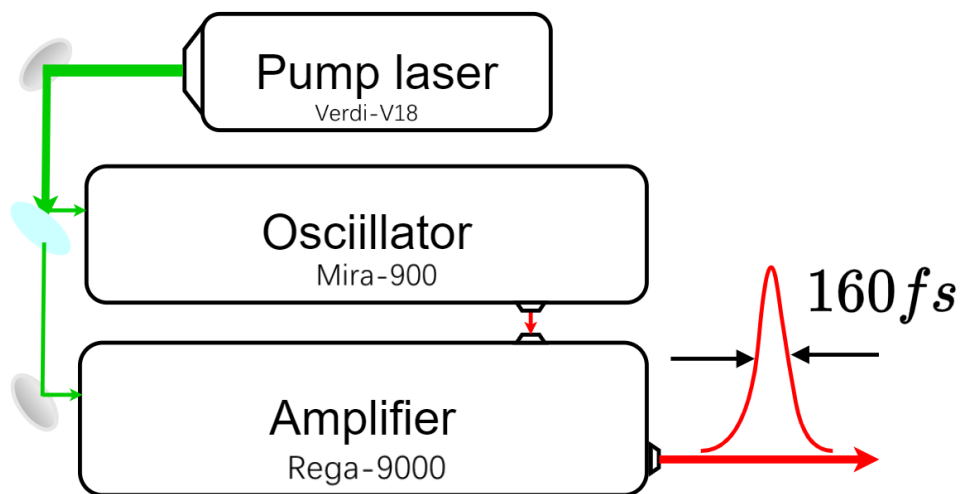

Figure 2.1 – femtosecond laser source schematic

The optical schematics of the three parts are shown below separately in **Figure 2.2,**
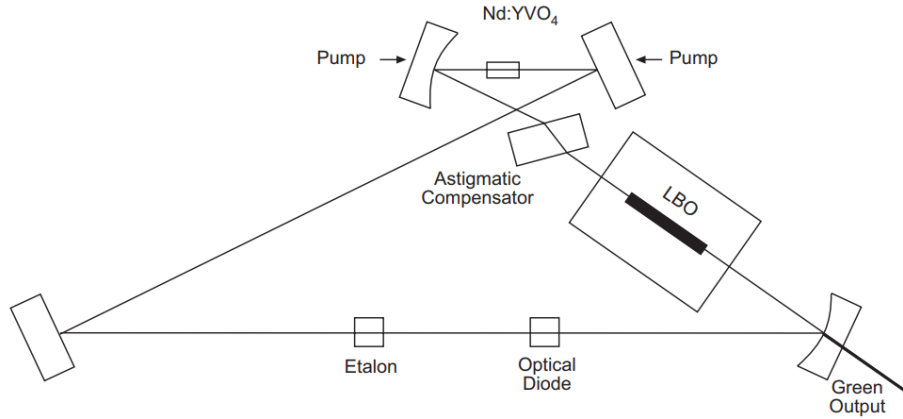
Figure 2.2(a) – Pump laser: Verdi-V18

Verdi-V18 Specifications [20]:

Output power: 17.5 W

Wavelength: 532 nm

Beam diameter: 2.25mm $\pm$10%

BP:	Brewster prism	L:	Focusing lens
BRF:	Birefringent filter	M:	Mirror
BS:	Beamsplitter	$TiAl_2O_3$:	Titanium:sapphire crystal

Figure 2.2(b) – Oscillator: Mira 900

Mira 900 Specifications [21]:

Average output power: 500 mW   Autocorrelation width: 200 fs

Femtosecond tunning range: 720-810 nm   Repetition rate: 76 MHz

Beam diameter at output coupler: 0.8mm$\pm$0.1

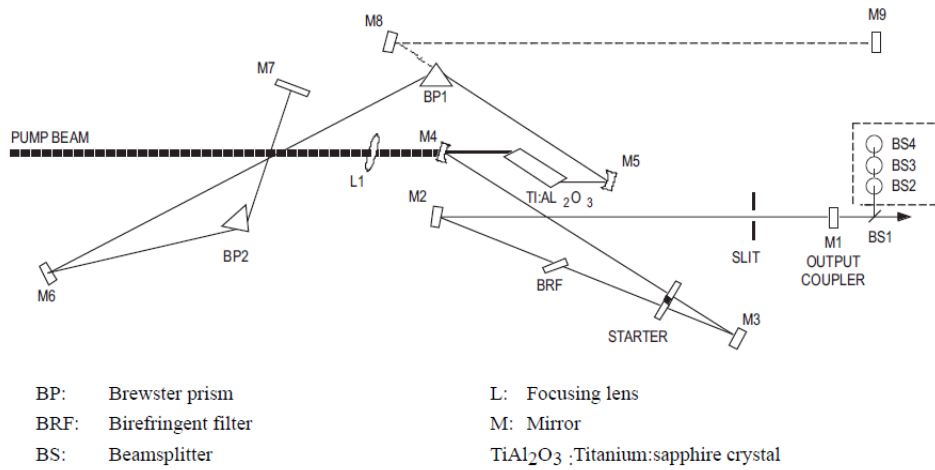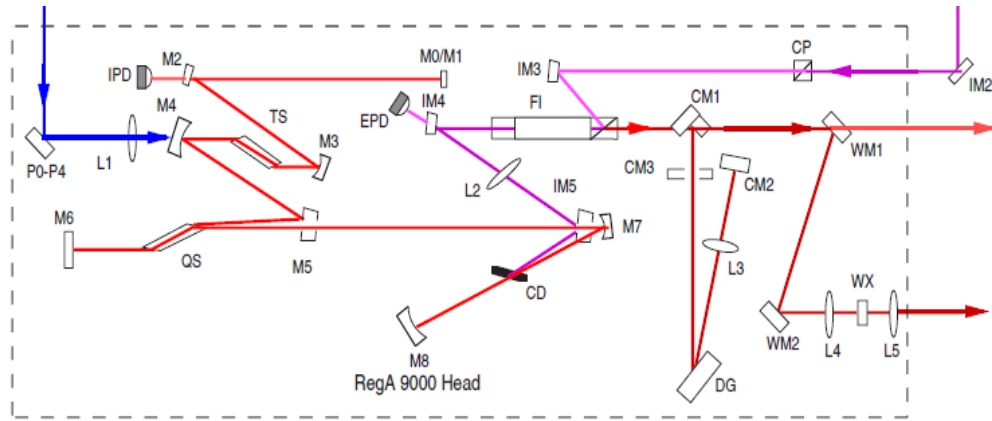| IB:	Ion Beamsplitter	WX:	White-Light Crystal
IPD:	Injection Photodiode	M0 - M8:	Cavity Optics
EPD:	Ejection Photodiode	IM1-IM5:	Injection Optics
QS:	Q-Switch	CM1-CM3:	Compressor Optics
CD:	Cavity Dumper	WM1 - WM2:	Whitelight Optics
FI:	Faraday Isolator	L0 - L5:	Lenses
CP:	Cube Polarizer	P0 - P4:	Pump Optics
DG:	Diffraction Grating	TS:	Ti:Sapphire Crystal

Figure 2.2(c) – Amplifier: Rega 9000

Rega 9000 Specifications [22]:

Pulse energy: 2 μJ   Repetition rate: 10 kHz to 300 kHz

Pulse duration: 160 fs   Beam diameter: 3 mm

Figure. 2.3 – A photograph of the laser source

13

2.1.2 Optical path

The primary purpose of constructing this optical path is to realize femtosecond laser pulse shaping and continuous duration control. Pulse duration measurement and adjustment can be achieved by second harmonic generation of sub-optical path and Brewster prism pairs compensation. The galvano mirror and filter can change the laser intensity and final sample ionization position. Actual optical schematic is shown in **Figure 2.4**
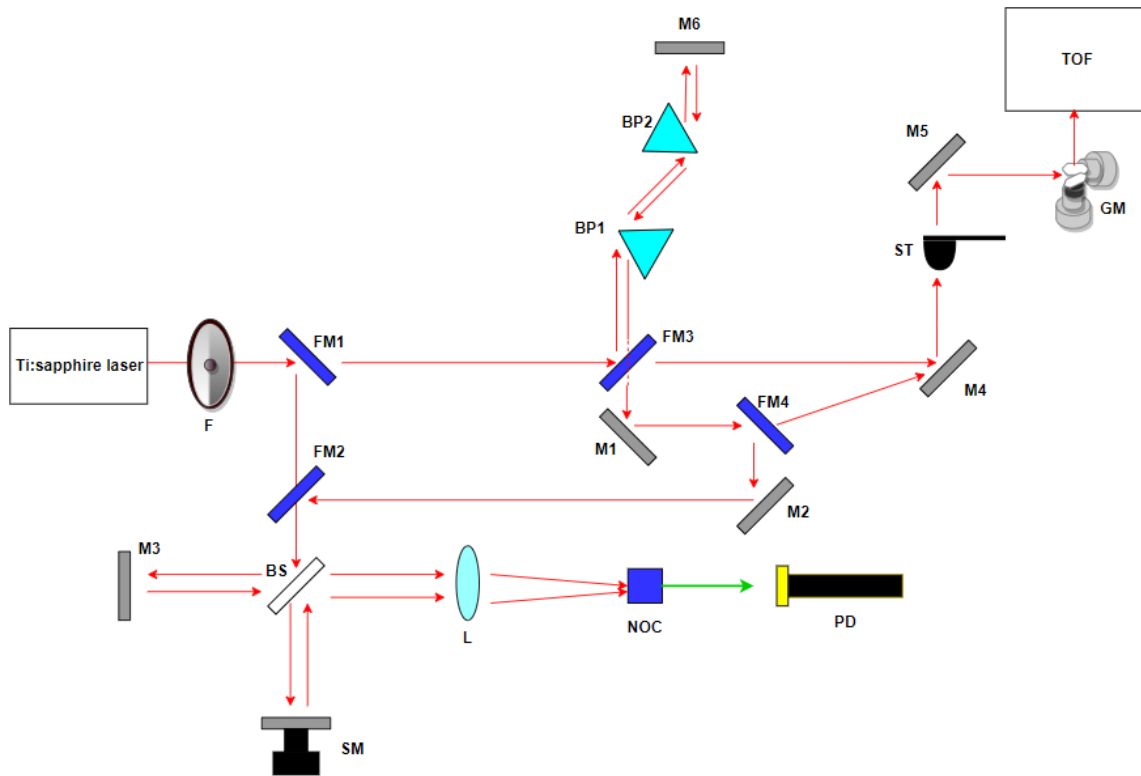
Figure 2.4 – Optical schematic

FM1-4: Foldable mirror   M1-6: Mirror

F: Filter   BP1-2: Brewster prism

L: Focusing lens   BS: Beam splitter

PD: Photodiode   ST: Shutter

SM: Stepping motor   NOC: Nonlinear optical crystal
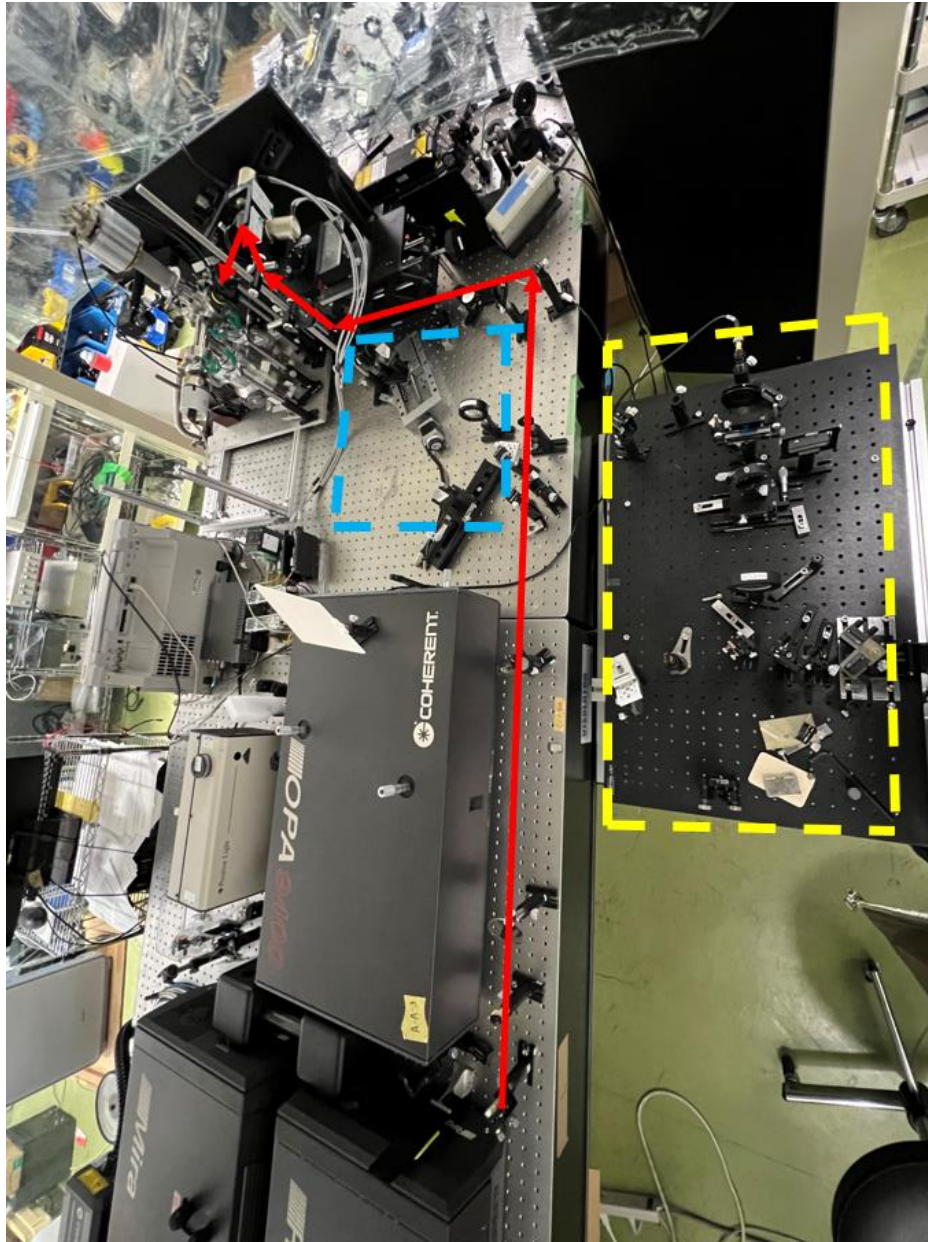
GM: Galvano mirror

Figure 2.5 – Photograph of the optical path

In **Figure 2.5**, the solid red line shows the optical path of the femtosecond laser. The prism pair's sub-optical path unit for pulse compression is shown in the blue dotted area. The yellow dotted line area shows the autocorrelation system for measuring pulse duration using second harmonic generation.
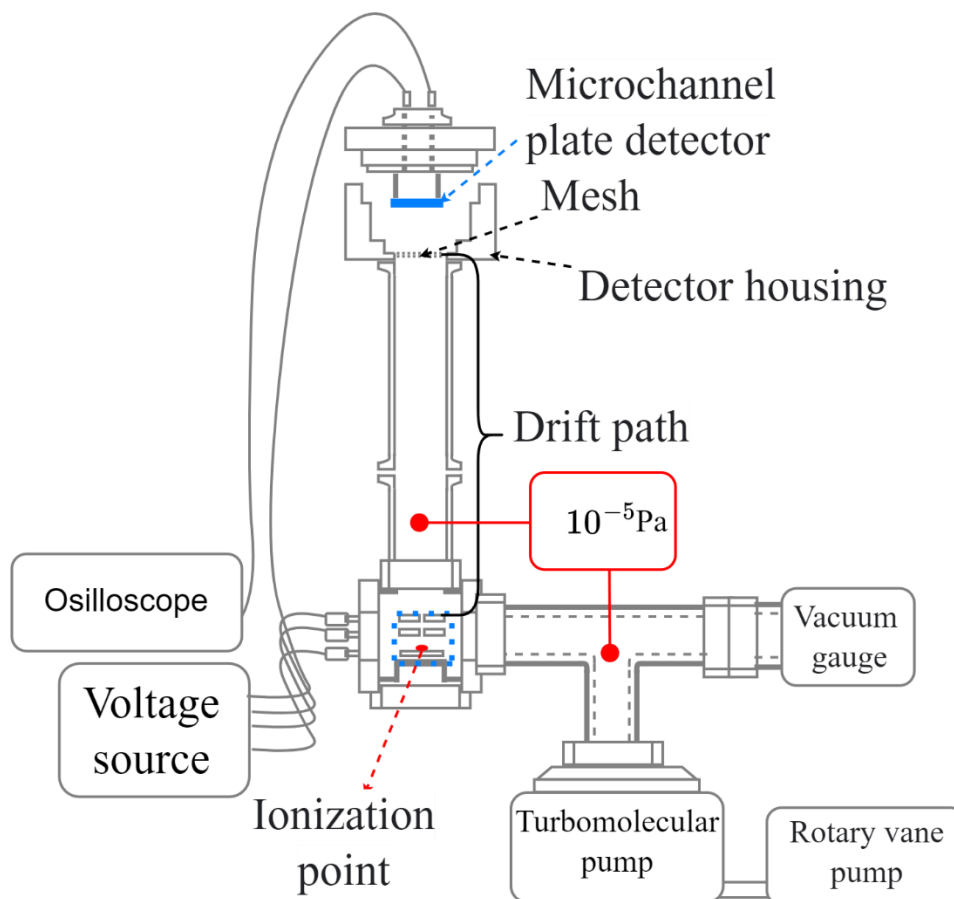
2.2 TOF mass spectrometer

Figure 2.6 –Schematic illustration of the TOF mass spectrometry system.

The general structure of the schematic of the TOF-MS system is shown in **Figure 2.6**. The femtosecond laser is focused onto the sample plate. And the sample is ionized by the laser light. The ions ionized by the laser light are accelerated by two-stage accelerating and enter the drift path region. In order to prevent the influence of the electric field created by the potential held to the micro-channel plate (MCP), a ground mesh was placed in front of the MCP. Ions hit an MCP and are converted into electric current and amplified. Then, the current is detected and analyzed by an oscilloscope. The internal vacuum of the whole system is maintained at 10^{-5} Pa. **Figure 2.7** shows a photograph of the system, which does not include the following: a rotatory vacuum pump, a power suply, and an oscilloscope.
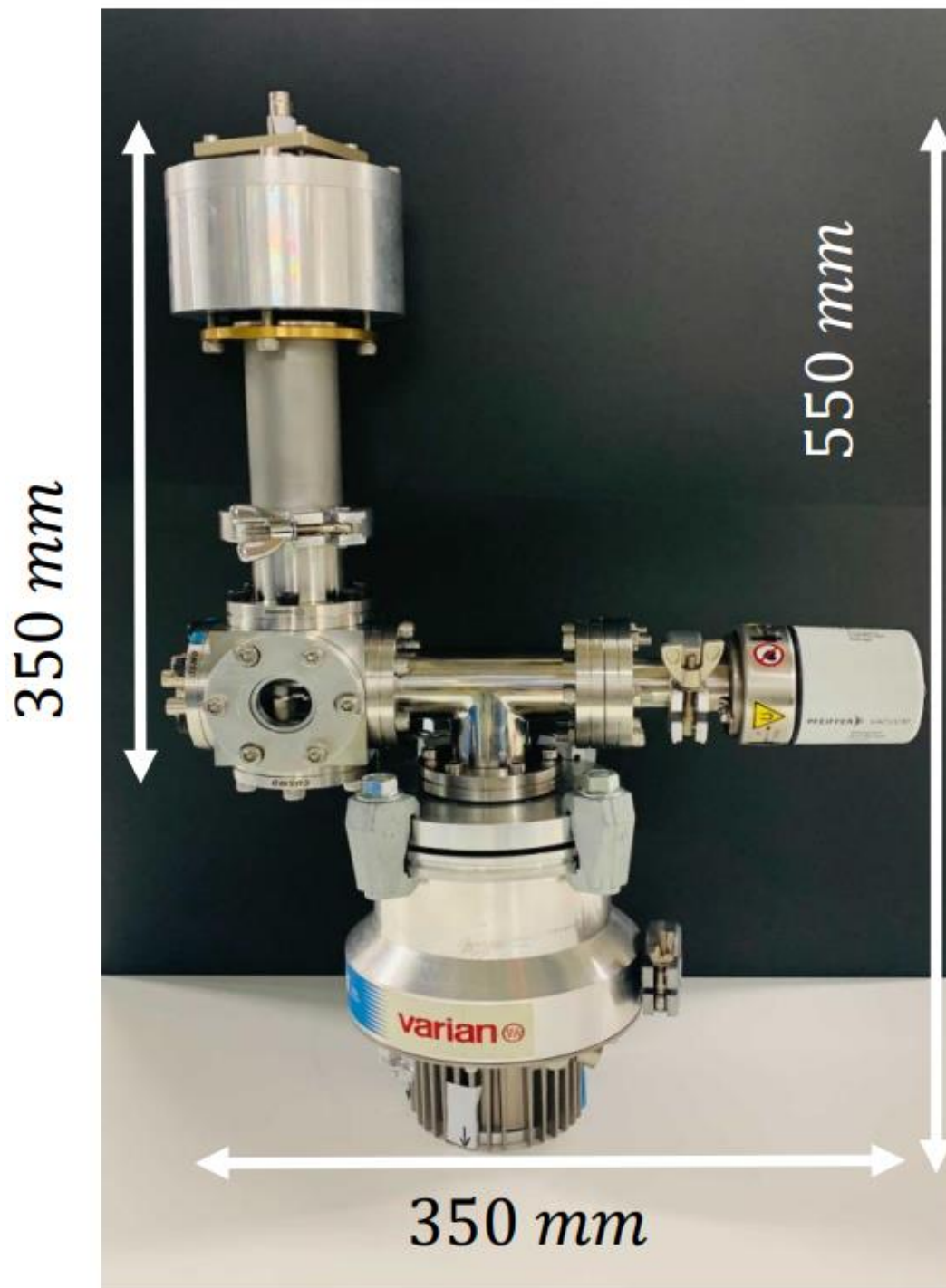
16

Figure 2.7 –A photograph of the TOF-MS system.

2.2.1 TOF-MS instrument

The CAD drawing of the TOF mass spectrometer instrument in the cross section and the internal electrode arrangement with actual dimensions are shown in **Figure 2.8** and **Figure 2.9,** respectively**.** The TOF mass spectrometer instrument is divided into three main parts: a two-stage acceleration ion source, a drift tube, and a detector.
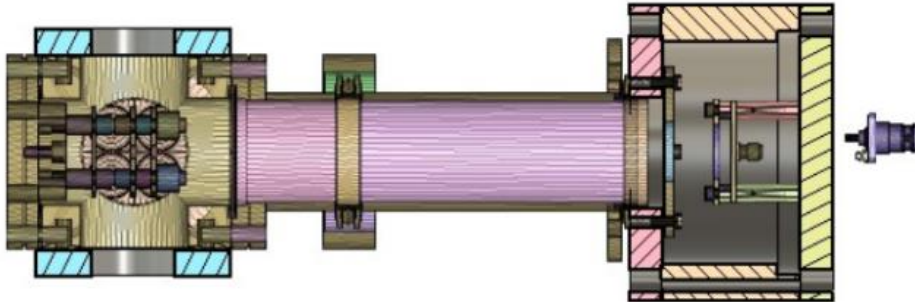
Figure 2.8 Cross-sectional view of the TOF-MS instrument

By CAD drawing.
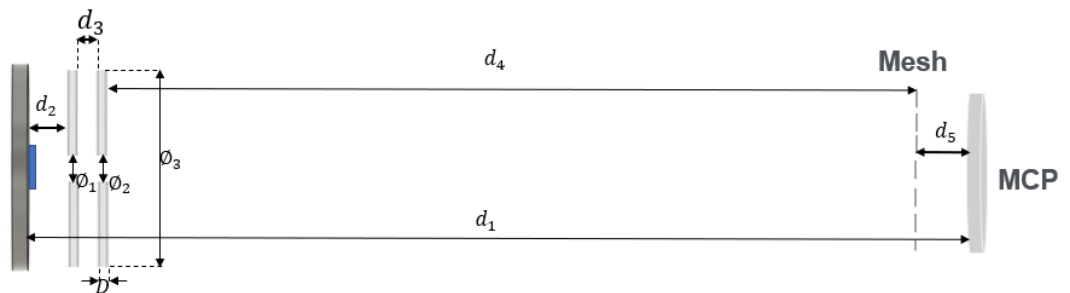
d_1=222.5mm

d_2=11mm

d_3=5.5mm

d_4=193mm

d_5=9mm

$\emptyset_1$=2.4mm

$\emptyset_2$=2.9mm

$\emptyset_3$=34mm

D=2mm

Figure 2.9 Diagram of the actual arrangement and dimensions of the electrode.

2.2.1.1 Two-stage acceleration electrodes

Figure 2.10 - Picture of two-stage acceleration electrodes (left) and
3D CAD drawing (right)

Two-stage acceleration electrodes part: The first stage is a first-order acceleration from the sample plate to the first aperture, followed by a second-order acceleration from the first to the second aperture and the final emitted from the second aperture to the drift tube.

2.2.1.2 Drift tube

To increase the drift path in the field-free region, a drift tube was used between the acceleration electrodes and mesh, internal radius: 42.7 mm, length: 100.0 mm, and material is stainless alloy.
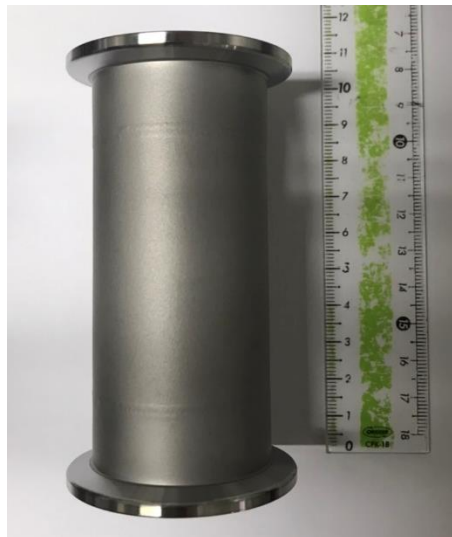

Figure 2.11 –Drift tube picture

2.2.1.3 Detector housing

The detection housing is mainly made up of the mesh and the MCP, shown in **Figure 2.12** and **Figure 2.13,** respectively**.** MCP of 20 mm diameter with center hole (F12334-11, Hamamatsu photonics, Japan)
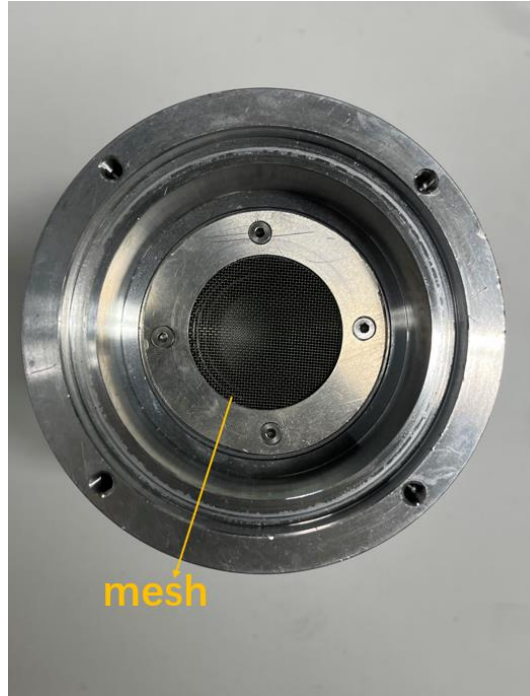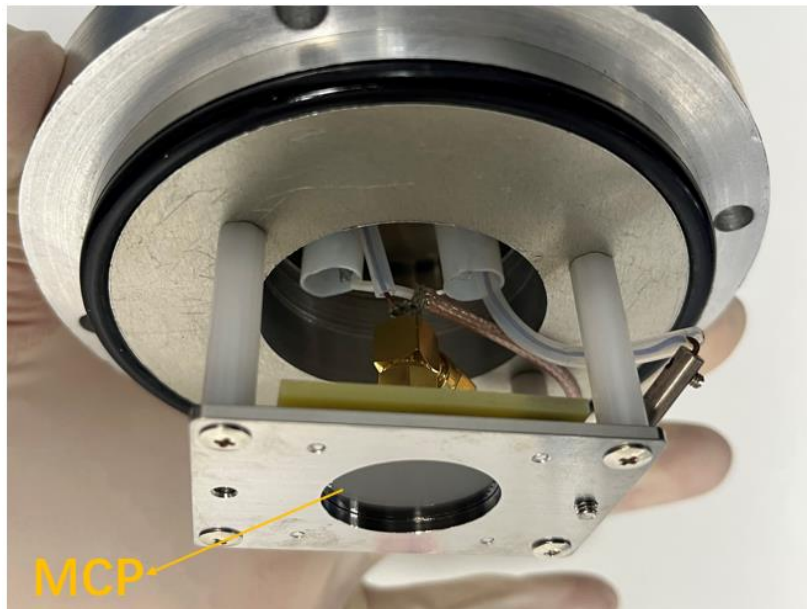

Figure 2.12 –Ground mesh inside the detector housing.

Figure 2.13 –The MCP detector inside the detector housing

3 System Simulation and Mechanisms

INTRODUCTION

This chapter introduces the physical mechanism and simulation of the experimental system, from the (1) pulse control of the femtosecond laser to the (2) sample ion kinetic energy distribution using femtosecond laser desorption/ionization, then the (3) TOF mass spectrometer electric potential distribution and ion trajectory control, to the final (4) ion detection and signal analysis. These processes are schematically shown in **Figure 3.1** and the numbers in the figure correspond to the respective processes. Each of these processes from (1) to (4) is described in the following sections, which are further divided into the following parts:
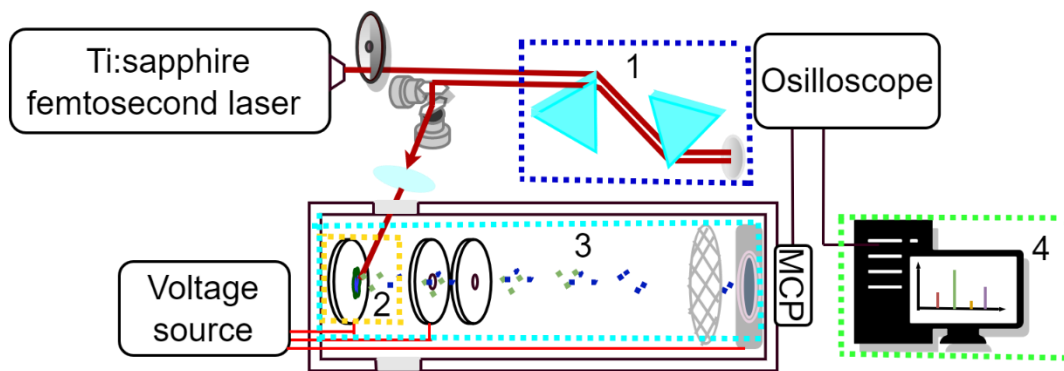
Figure 3.1 – Schematic of the experimental system

- Electric potential simulation
- Ion trajectory simulation
- Laser pulse control
- Ion kinetic energy distribution in femtosecond laser ionization
- Deriving initial velocity distribution from signal
- Conclusion and conception

For the electric potential simulation part, to check the simulation stability I used three different simulation methods to simulate potential distribution in the same system, then compared the final simulation results with each other. After the potential distribution of

the system is obtained, the electric field and ion trajectories under the potential distribution are simulated and inspected according to the optimization method of each method. The laser pulse control part introduced the mechanism of femtosecond laser pulse compression and theoretical calculation. Ion kinetic energy distribution in femtosecond laser ionization selected the shifted-MB distribution as the model to simulate the emitted ions energy distribution.

3.1   Electric potential simulation

The development of electrostatic lens theory began in the 1930s, from the earliest of the paraxial approximate ray equation and then to the Laplace equation based on the Bessel equation of the multi-series expansion. For the electrostatic lens system of two apertures we used, the potential distribution and focusing properties are shown in **Figure 3.1.1** The equipotential lines between the two electrodes are marked by the red dashed line, the green arrows represent the direction of the electric field lines according to the relationship between the electric field lines and perpendicular to the equipotential lines. Therefore, between the two electrodes, the ion will first be subjected to the force of focusing to the center and then to the force of defocusing from the center, through a reasonable distribution of the voltage of the two electrodes to achieve a good focusing effect. In this case, the ions follow the trajectory shown by the blue line in Figure 3.1.1. through the apertures. To improve the performance of a two-aperture electrostatic lens system to obtain a better detection signal resolution in space and time, the potential distribution in the system must be reasonably adjusted to achieve high-precision ion trajectory control. Therefore, numerical simulation is used to estimate the spatial distribution and motion of ions to achieve a better ion beam focusing effect.
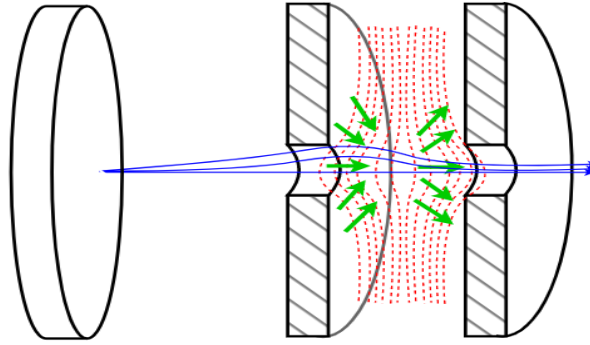
Figure 3.1.1 – Paths of ions in a
two-aperture electrostatic lens (cross-section)

3.1.1   Surface charge method [23]

The surface charge method is flexible, which can change the distribution of contour points according to the electrode shape and the precision requirement. For an electrode of arbitrary geometry, the surface can be divided into n contour points S_n, each contour point S_n corresponds to an imaginary charge q_n which under the electrode surface. The structure is shown in **Figure 3.1.2**,
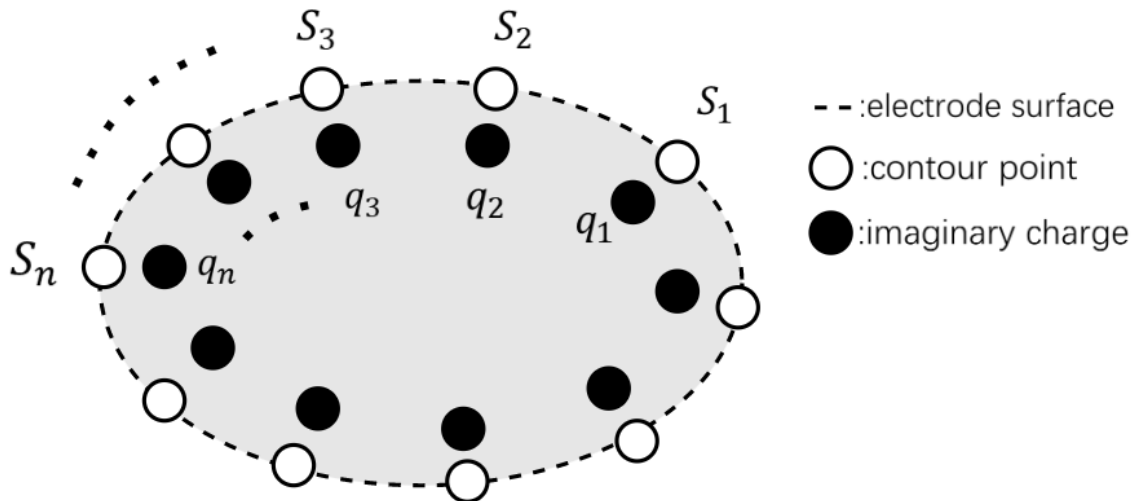
Figure 3.1.2 – Surface charge method

The imaginary charges under the surface electrode will substitute the actual charges on the electrode surface and generate a potential effect the same as the actual charges. Therefore, it is also called the substitute charge method. When the imaginary charges are distributed under the electrode, and the superposition of the electric field effect generated

by the imaginary charges satisfies the boundary condition of the electrode voltage, the corresponding imaginary charges can be calculated. Thus, the potential at contour point S_i generated by all imaginary charges q_n can be defined as

$$\emptyset_i = \sum_{j=1}^{n} \frac{1}{4\pi\varepsilon_0} \frac{q_j}{r_{i,j}} \tag{3.2}$$

in which $r_{i,j}$ is the distance between the contour point S_i and imaginary charge q_j. Therefore, the value of q_n imaginary charges can be solved by matrix form,

$$\frac{1}{4\pi\varepsilon_0}\begin{pmatrix} r_{1,1}^{-1} & r_{1,2}^{-1} & \cdots & r_{1,j}^{-1} \\ r_{2,1}^{-1} & \ddots & & \vdots \\ \vdots & & \ddots & \vdots \\ r_{i,1}^{-1} & \cdots & \cdots & r_{i,j}^{-1} \end{pmatrix}\begin{pmatrix} q_1 \\ q_2 \\ \vdots \\ q_n \end{pmatrix} = \begin{pmatrix} V_1 \\ V_2 \\ \vdots \\ V_n \end{pmatrix} \tag{3.2}$$

formed by the S_n contour points' boundary conditions. $V_1 \sim V_2$ are electrodes' voltage boundary conditions.

Then the potential and electric field of the vector point R in space can be derived by the superposition effect of q_j imaginary charges

$$\emptyset(R) = \sum_{j=1}^{n} \frac{1}{4\pi\varepsilon_0} \frac{q_j}{|R-r_j|}, \tag{3.3a}$$

$$E(R) = \sum_{j=1}^{n} \frac{1}{4\pi\varepsilon_0} \frac{q_j}{|R-r_j|^3}. \tag{3.3b}$$

The actual effect of the imaginary image can be seen in **Figure 3.1.3**
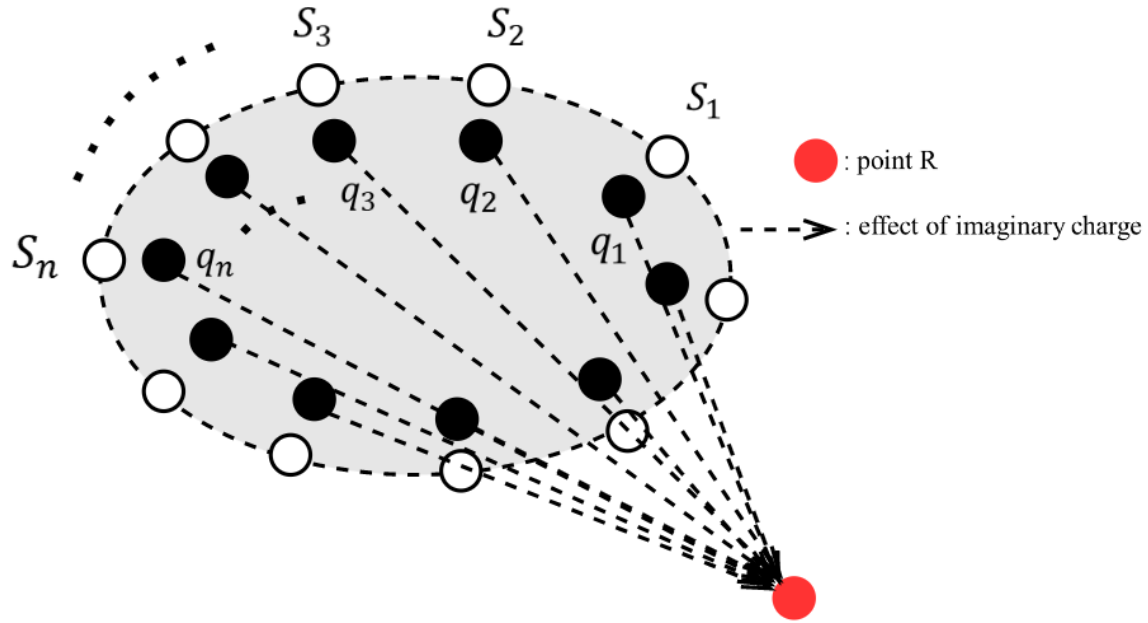
Figure 3.1.3 –Charge superposition effect.

The calculation accuracy of the surface charge method can be effectively improved by adjusting the position and density of the contour point [24]. More contour points need to be distributed for where the electric field changes dramatically or for some essential parts. Especially for the corner electrode structure or some precise convex and concave structure shown in **Figure 3.1.4**, it is necessary to pay attention to the contour point distribution.

Figure 3.1.4 –Convex and concave structure.

The distance relationship of length a: between the imaginary charge and the corresponding contour point, and length b: distance between the two adjacent contour points also must be considered, as shown in **Figure 3.1.5**,
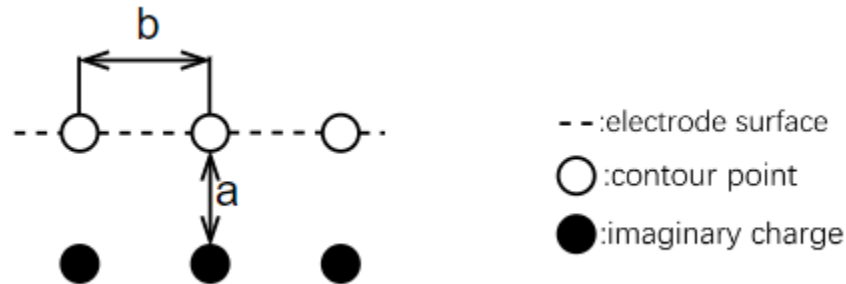
Figure 3.1.5 –Schematic diagram of the positional relationship between contour points and

imaginary charge.

It is necessary to choose a proper ratio between a and b to balance and avoid the fluctuation of the equipotential line on the electrode surface. Let the ratio f be defined as

$$f = \frac{a}{2b},$$
(3.4)

When f is too small, the structure of the electrode cannot be correctly simulated, resulting in a low potential on the surface. On the other hand, if f is too large, it will cause the potential at the electrode surface to fluctuate, as shown in **Figure 3.1.6;** both of these conditions will cause errors in the simulation results.

Figure 3.1.6 – f effect on the surface potential

Therefore, the selection of appropriate f can better fit the actual potential distribution, and reasonably adjust the density of contour points to reduce the calculation time of a gigantic matrix and improve the overall simulation efficiency. Generally, the value of f depends on the structure of the system, ranging from 0.2 to 1.5. For the smooth and large size structure, if wi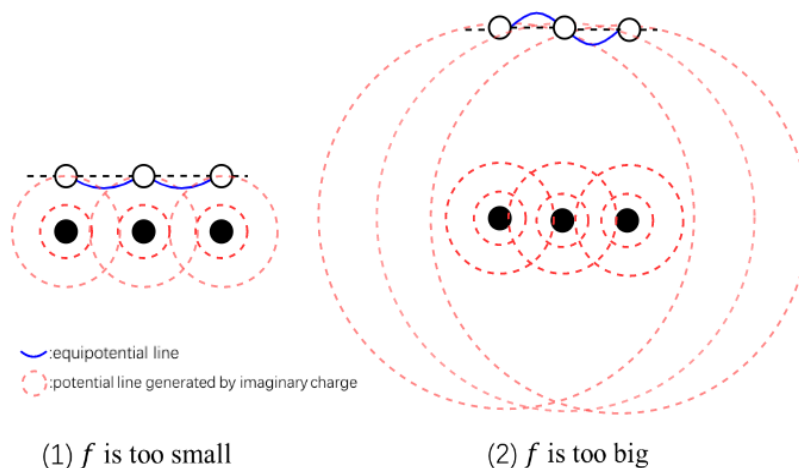thout a tip and protruding parts the f is about 0.5. For precise or important parts f is about 1.0. Normally the value can choose 0.75 [18].

3.1.2 Bessel function method [25]

For the case of an axisymmetric cylinder electrode system, Laplace's equation is defined as

$$\frac{\partial^2 V(r,z)}{\partial z^2} + \frac{1}{r}\frac{\partial}{\partial r}\left(r\frac{\partial V(r,z)}{\partial r}\right) = 0. \tag{3.5}$$

$V(r,z)$ is the potential. Using the separate function can divide it into two parts and add a constant term C

$$V(r,z) = Z(z)R(r) + C, \tag{3.6}$$

where $Z(z)$ and $R(r)$ separately represent the z axial and r radial coordinates. Substitute (3.6) into (3.5) and express them in a general solution type

$$Z(z) = A_k e^{kz} + B_k e^{-kz}, \tag{3.7a}$$

$$R(kr) = D_1 J_0(kr) + D_2 Y_0(kr), \tag{3.7b}$$

where $J_0(kr)$ is Bessel function with zero-th order of first kind and $Y_0(kr)$ is zero order of second kind. Because the $Y_0(kr)$ is approaching to infinity at $r = 0$, so there is a singularity and we have to set constant $D_2 = 0$ to avoid it. The general solution will become

$$V(z,r) = (A_k e^{kz} + B_k e^{-kz})J_0(kr) + V_0, \tag{3.8}$$

where k can be calculated out when $J_0(kr)$ equal to 0, the general constant solution of the Bessel function is already known in some Python SciPy database. Therefore, the general solution for $V(z,r)$ will consist of a sum of k_n. Then the boundary conditions of potential and cylindrical size can be used to determine the unknown coefficients of the general solution A and B. **Figure 3.1.7** shows two coaxial cylinders with the same radius R and a gap g in the center. When the left and right electrodes voltage are held potentials of V_1

and V_2, the potential distribution in the center regions I , III and the gap region II can be expressed separately by (3.8). In the region I and III , if the electrode length is too long along the $\pm z$ axis, the exponential term $e^{\pm kx}$ will become infinite, therefore only one term has physical meaning. The potential distributions of the three regions are written as follows.
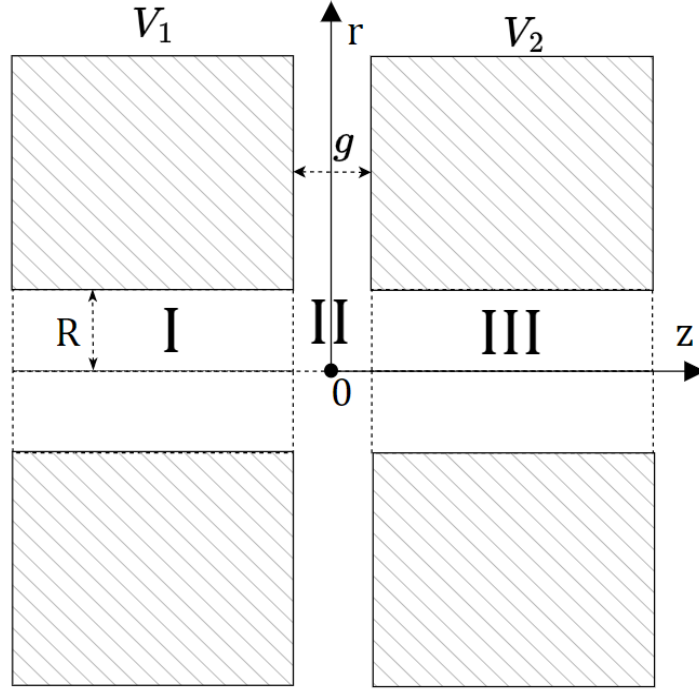
Figure 3.1.7 - Structure of two coaxial cylinders

I , III and gap region II,

$$V_{\text{I}}(z,r) = V_1 + \sum_{n=1}^{\infty} A_n e^{k_n z} J_0(k_n r) \tag{3.9a}$$

$$V_{\text{II}}(z,r) = \frac{V_1+V_2}{2} + \left(\frac{V_2-V_1}{g}\right) z + \sum_{n=1}^{\infty} (B_n e^{-k_n z} + B'_n e^{k_n z}) J_0(k_n r) \tag{3.9b}$$

$$V_{\text{III}}(z,r) = V_2 + \sum_{n=1}^{\infty} C_n e^{-k_n z} J_0(k_n r) \tag{3.9c}$$

Since it is a symmetric system and the region I , II and III are continuously in the boundary $z = \pm\frac{g}{2}$, so the coefficients satisfy the following relation.

28

$$\begin{cases} A_n = -C_n \\ B_n = -B_n' \\ A_n e^{\frac{-k_n g}{2}} = \left(B_n e^{\frac{k_n g}{2}} + B_n' e^{-\frac{k_n g}{2}} \right). \\ C_n e^{\frac{k_n g}{2}} = \left(B_n e^{-\frac{k_n g}{2}} + B_n' e^{\frac{k_n g}{2}} \right) \end{cases} \qquad (3.10)$$

Substitute (3.10) into the equations and simplify to the following form

$$V_{\mathrm{I}}(z,r) = V_1 + \sum_{n=1}^{\infty} B_n [e^{k_n g} - 1] e^{k_n z} J_0(k_n r) \qquad (3.11\mathrm{a})$$

$$V_{\mathrm{II}}(z,r) = \frac{V_1 + V_2}{2} + \left(\frac{V_2 - V_1}{g} \right) z + \sum_{n=1}^{\infty} B_n (e^{-k_n z} - e^{k_n z}) J_0(k_n r) \qquad (3.11\mathrm{b})$$

$$V_{\mathrm{III}}(z,r) = V_2 - \sum_{n=1}^{\infty} B_n (e^{k_n g} - 1) e^{-k_n z} J_0(k_n r) \qquad (3.11\mathrm{c})$$

The electrostatic field energy density can be calculated by

$$U_E = \frac{1}{2} \epsilon_0 E^2. \qquad (3.12)$$

Because physical systems will adjust their conditions to achieve a minimum potential energy. For the total energy in the three regions I , II and III , considering symmetry and ease of calculation, we just consider the energy of a quarter region and use the variational principle.

$$W = \pi \epsilon_0 \int_{-\infty}^{-\frac{g}{2}} \int_0^R \left[\left(\frac{\partial V_{\mathrm{I}}}{\partial z} \right)^2 + \left(\frac{\partial V_{\mathrm{I}}}{\partial r} \right)^2 \right] r \, dr \, dz + \qquad (3.13)$$

$$\pi \epsilon_0 \int_{-g/2}^{0} \int_0^R \left[\left(\frac{\partial V_{\mathrm{II}}}{\partial z} \right)^2 + \left(\frac{\partial V_{\mathrm{II}}}{\partial r} \right)^2 \right] r \, dr \, dz].$$

$$\frac{\partial W}{\partial B_n} = 0. \qquad (3.14)$$

By solving these two equations, we can get the solution of B_n

$$B_n = \frac{(V_2 - V_1) e^{-\frac{k_n g}{2}}}{g R k_n^2 J_1(k_n R)}, \qquad (3.15)$$

where $J_1(k_n R)$ is first kind Bessel function with one order, with the known R the corresponding solutions can directly be obtained from mathematical databases, or Python, etc. Then we can substitute B_n into the expression for the three regions to find the potential distribution in the three regions.

3.1.3   The relaxation method

Laplace's equation can also be replaced by differential equations, and then solved them by approximating derivatives with finite differences based on relaxation method (also known as Jacobi's method). The advantage of this method is that we can use simple coding and do not need an additional external database. Differently from the surface charge method, which divides electrodes into discrete contour points, the relaxation method directly divides the entire potential space into discrete lattice points, and then by using the differential equation form instead of the Laplace equation to solve and simulate the cylindrical electrostatic lens system. Cylindrical polar coordinates Laplace's equation can be written from (3.5) to

$$\frac{\partial^2 V}{\partial z^2} + \frac{\partial^2 V}{\partial r^2} + \frac{1}{r}\frac{\partial V}{\partial r} = 0. \tag{3.16}$$

With Taylor's expansion of the interval h we can express as

$$V(z, r + h) = V(z, r) + h\frac{\partial V}{\partial r} + \frac{1}{2}h^2\frac{\partial^2 V}{\partial r^2} + \frac{1}{6}h^3\frac{\partial^3 V}{\partial r^3} + \cdots, \tag{3.17a}$$

$$V(z + h, r) = V(z, r) + h\frac{\partial V}{\partial z} + \frac{1}{2}h^2\frac{\partial^2 V}{\partial z^2} + \frac{1}{6}h^3\frac{\partial^3 V}{\partial z^3} + \cdots. \tag{3.17b}$$
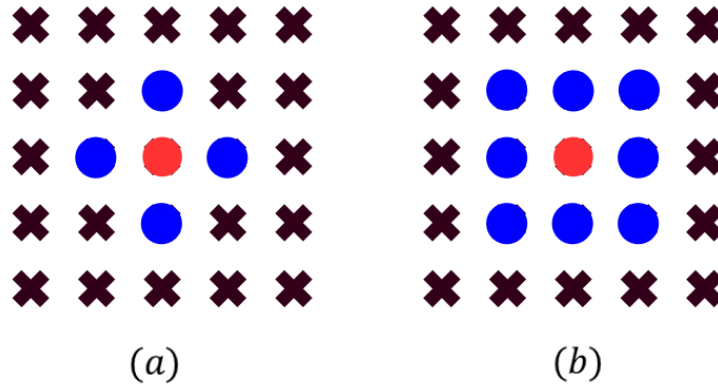

(a) (b)

Figure 3.1.8 – (a)five points case(b)nine points case

After getting the above equations, the target red point potential can be solved with the surrounding points of five-point and nine-point cases. For the five-point relaxation method case, using the center derivative method based on the potential of the center point

30

$V(z, r)$ and surrounding four points ($V(z \pm h, r)$ and $V(z, r \pm h)$) we can get 2_{nd} order accuracy of series expansion as

$$V(z - h, r) + V(z + h, r) + V(z, r - h) + V(z, r + h) - 4V(z, r)$$
$$= h^2\left(\frac{\partial^2 V}{\partial r^2} + \frac{\partial^2 V}{\partial z^2}\right) \quad (3.18a)$$

$$\frac{h}{2r}\left(V(z, r + h) - V(z, r - h)\right) = \frac{h^2}{r}\frac{\partial V}{\partial r} . \quad (3.18b)$$

By solving (3.18a), (3.18b) and (3.16) together, we can express $V(z, r)$ as

$$V(z, r) = [V(z - h, r) + V(z + h, r) +$$
$$(1 + \frac{h}{2r})V(z, r - h) + (1 - \frac{h}{2r})V(z, r + h)]/4. \quad (3.19)$$

However, this equation cannot solve the potential at the center of the axis $r = 0$, because $\frac{h}{2r}$ term would become infinity. Therefore, the potential point of $V(z, 0)$ takes 6 points to decide it, each along the front and back of the target point, and four points are in a plane perpendicular to the axis and can be written as

$$V(z, 0) = [V(z - h, 0) + V(z + h, 0) + 4V(z, h)]/6. \quad (3.20)$$

To optimize and improve the relaxation convergence speed, especially for some big systems that need more lattice points to cover the potential space, we can use the Simultaneous over relaxation method [25], one obtains

$$V(z, r) = \frac{\omega}{4}[V(z - h, r) + V(z + h, r) + (1 + \frac{h}{2r})V(z, r - h) +$$
$$(1 - \frac{h}{2r})V(z, r + h)] - (\omega - 1)V^\dagger(z, r) \quad (3.21a)$$

$$V(z, 0) = \frac{\omega}{6}[V(z - h, 0) + V(z + h, 0) + 4V(z, h)]$$
$$- (\omega - 1)V^\dagger(z, r). \quad (3.21b)$$

For the case of the nine-point relaxation method as shown in **Figure 3.1.8**, four additional points are taken into account when the given weights are satisfied [26].

$$V(z, r) = [6(16r^2 + 7h^2)\left(V(z + h, r) + V(z - h, r)\right)$$
$$+ (96r^2 + 30h^2 + 48rh + 23h^3/r)V(z, r + h)$$

$$+(96r^2+30h^2-48rh-23h^3/r)V(z,r-h)$$
$$+(24r^2+9h^2+12rh+13h^3/2r)V(z+h,r+h)$$
$$+V(z+h,r+h)$$
$$+(24r^2+9h^2-12rh-13h^3/2r)V(z-h,r-h)$$
$$+V(z+h,r-h)]/(60(8r^2+3h^2)) \tag{3.22}$$

$$V(z,0) = [34V(z,h)+5(V(z-h,0)+V(z+h,0))$$
$$+7(V(z-h,h)+V(z+h,h))]/58. \tag{3.23}$$

3.1.4   The applicability range of the three methods and comparison

The three methods described above were programmed in Python to check their validity and applicability to each other. For the two coaxial cylinders structure as shown in **Figure 3.1.9**. Regard the gap center of the two cylindrical electrodes as the origin of coordinates. The potentials of the two electrodes are 100V and 0V, respectively. Finally, compare the potential distribution of the *z*-axis and *r*-axis between the gap region of the two electrodes.
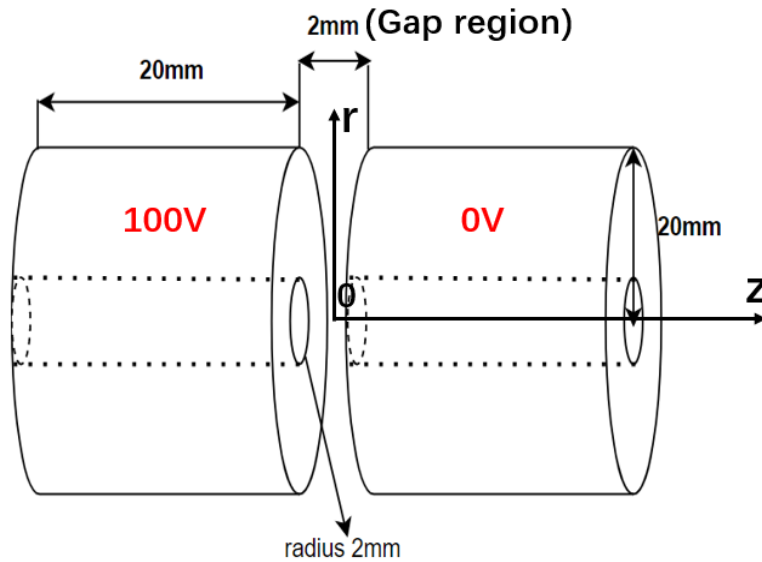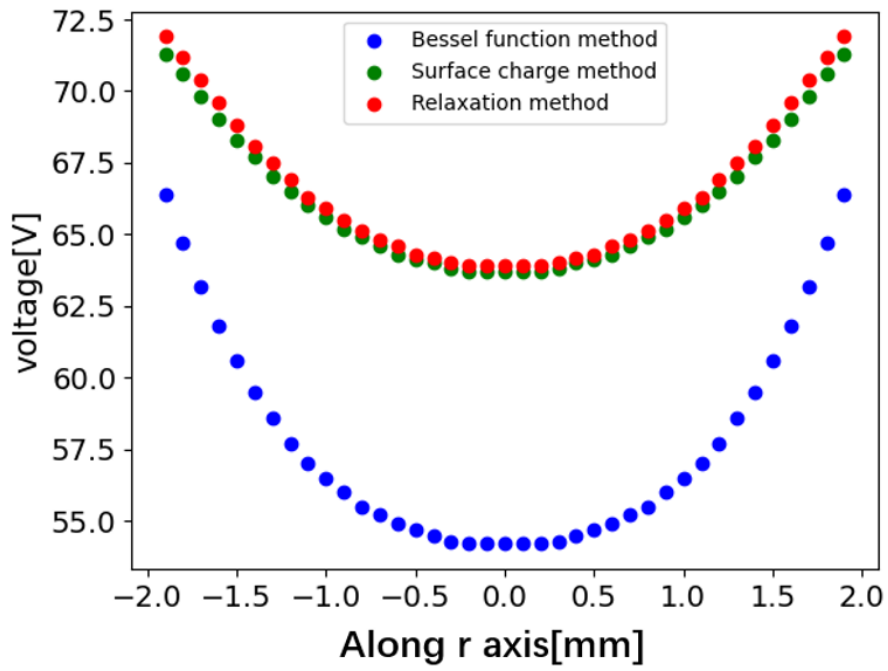

Figure 3.1.9 – Test two coaxial cylinders structure

32

a – Potential along *r* axis with three methods
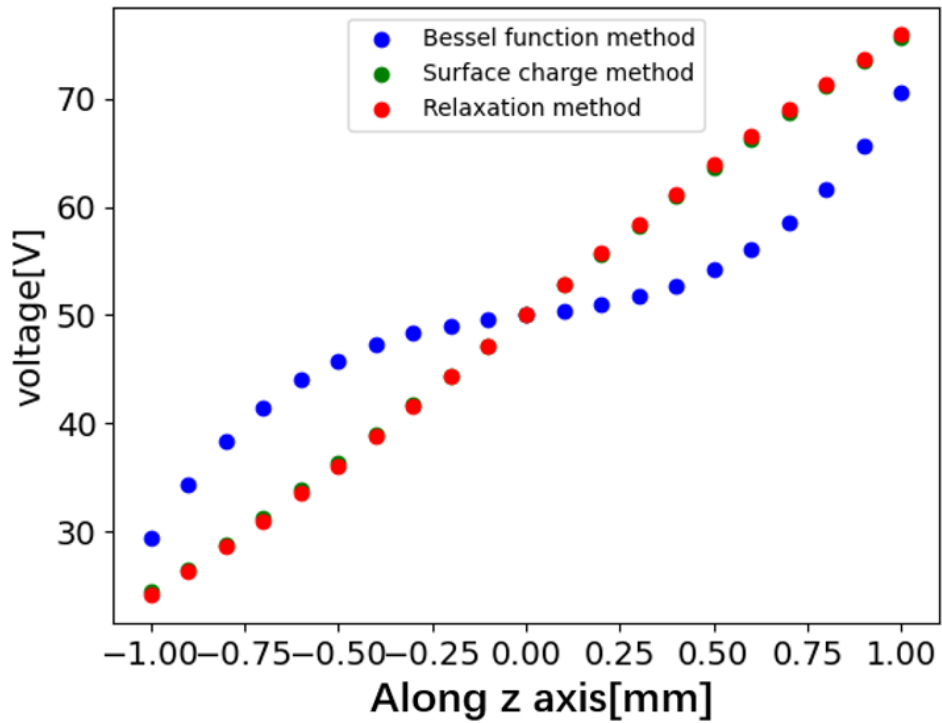
b – Potential along the *z*-axis with three methods

Figure 3.1.10

It can be seen from **Figure 3.1.10** that the results of the surface charge method and the Relaxation method are relatively close, but the difference between the Bessel method and the other two methods is considerable. The voltage difference in the peak part exceeds 10 V along the *r* axis. Compare the surface charge method and the relaxation method outcome.
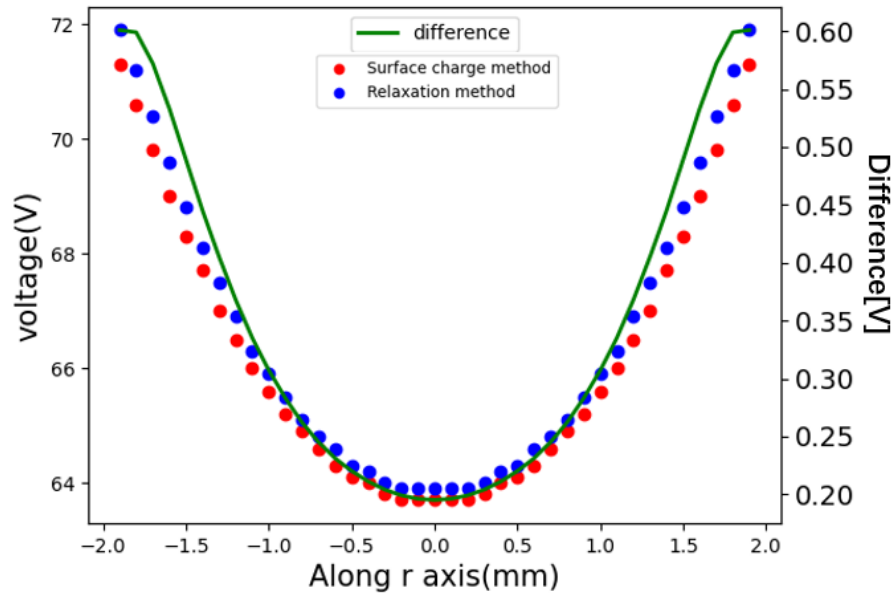
a– Potential along r axis with two methods
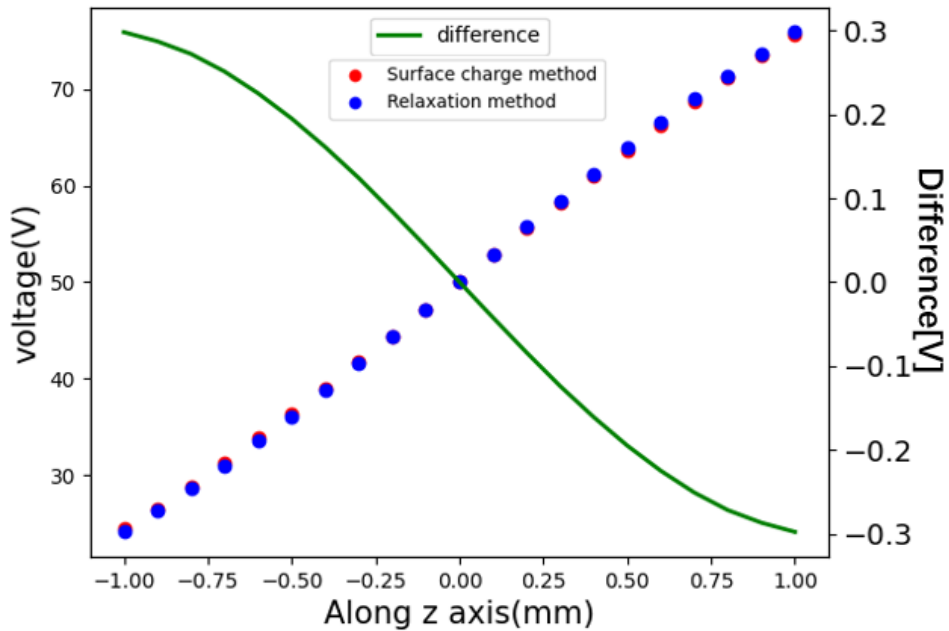
b– Potential along z axis with two methods

Figure 3.1.11

A detailed comparison of the difference in electrostatic potential between the surface charge method and the relaxation method shows that the difference is less than 0.6% in the *r*-axis direction and less than 0.3% in the *z*-axis direction. **Figure 3.1.11a** shows the voltages obtained by each method and their differences for the *r*-axis direction, and **Figure 3.1.11b** shows those for the *z*-axis direction. Considering that the deviation between the two simulation results is small, but the Bessel equation method in this structure exists a big discrepancy.

As an analytical solution of the cylinder electrode structure, the Bessel expansion method has no specific applicable restrictions, and there are boundary approximation steps and transformations in the derivation process. Confirmed the stability of the relaxation method with the surface charge method; in order to find out possible errors or specific application ranges of the Bessel function method, I chose the relaxation method to check and search it.

Through the comparison of the electric potential under the cylindrical structure of different sizes, finally the relaxation method and the Bessel method achieved good fitting results when the following structure was chosen as in **Figure 3.1.12.**
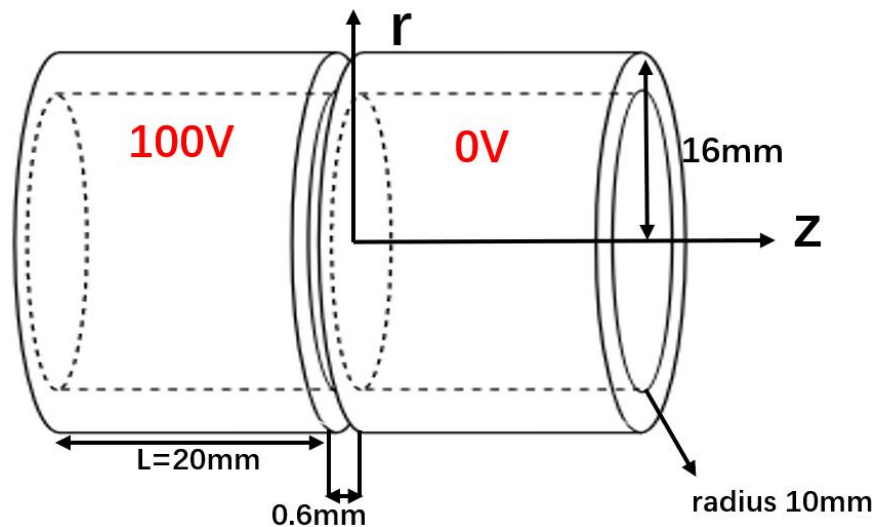
Figure 3.1.12 – Bessel method fitting structure
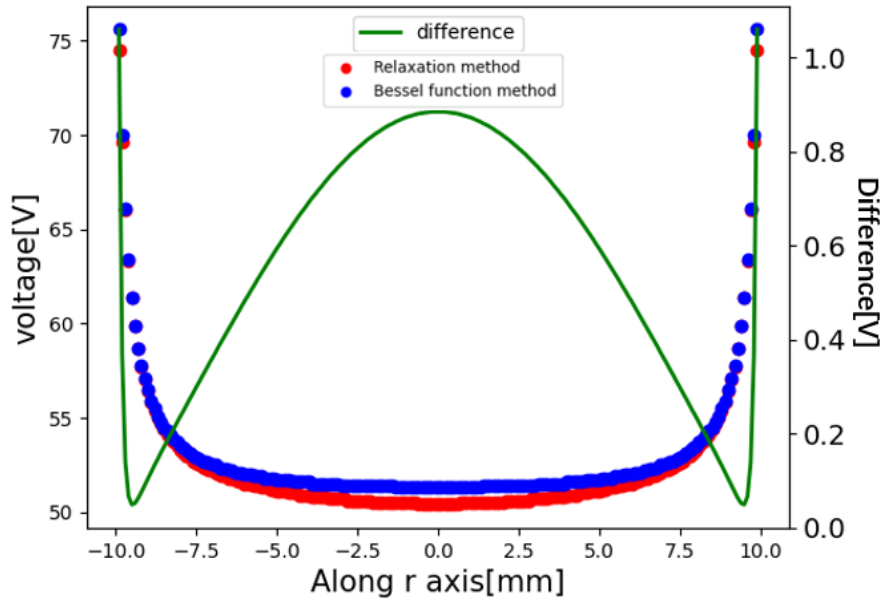
a – Potential along z axis
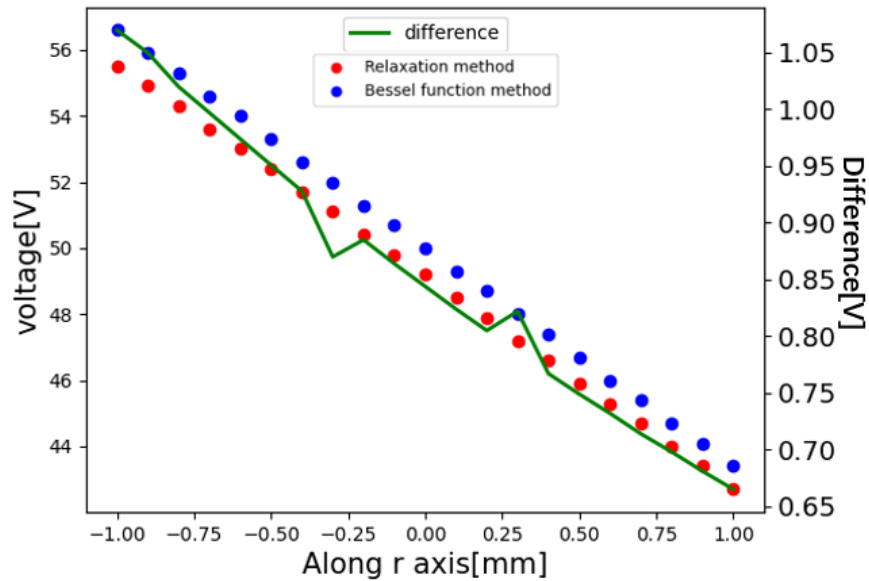
b – Potential along r axis

Figure 3.1.13

Compared to the fitting results of the former structure in **Figure 3.1.13**, the potential difference between the Bessel function method and the relaxation method is reduced from the peak value of 10 volts to about 1 volt. However, the service conditions of the Bessel function are also restricted, the gap distance of 0.6 mm is negligible compared to the cylinder length $L = 20$ mm, the aperture radius of 10 mm is also considerable for the

whole plate size of 16 mm. But the actual electrostatic lens system size: length of the cylinder $L = 2$ mm, and aperture size 2 mm, in contrast, the gap between the two plates is 5.5 mm. Due in the application range of the difference to Bessel equation, the surface charge method and the relaxation method will be used the most in the later potential simulation.

3.2 Trajectory simulation

3.2.1 Electric field calculation

In this part, ion trajectory simulation for the experimental setup is described. The area simulated by the numerical method starts from the sample plate to the end of the second aperture plate, then the later area is field free, and finally the linear acceleration area from the mesh to the MCP, the simplified TOF system electrode sketch is shown in **Figure 3.2.1**. $V_1 = 3000$ V, $V_2 = 2700$ V, MCP $=-1600$ V ,and the second aperture and mesh are grounded.
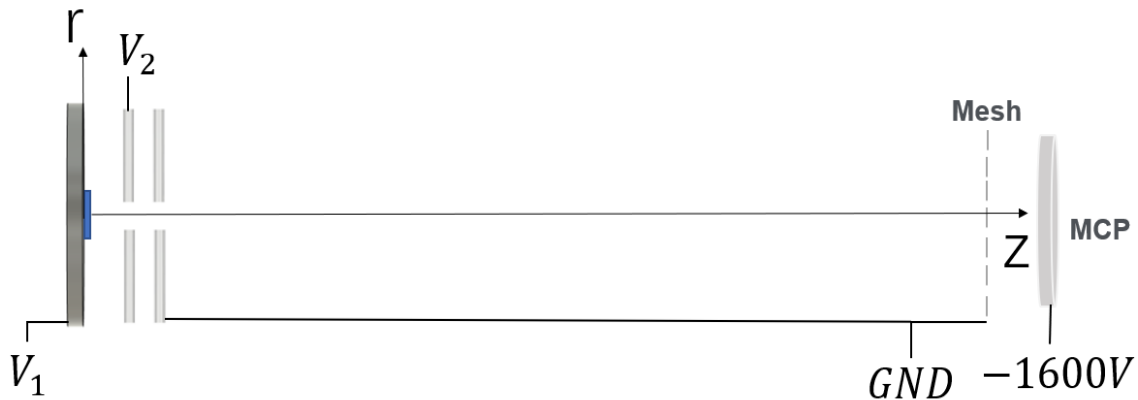
Figure 3.2.1 – TOF system electrode sketch

By comparing the results of the potential simulation distribution, the next step electric field calculation and ion trajectory simulation are performed using the numerical method of the surface charge method and the simultaneous over relaxation method. Although the surface charge method can directly calculate the potential and electric field at any position in space through the potential superposition effect of all imaginary charges. However, during the simulation of the ion trajectory, after each time interval Δt will take a long time for the ion when it reaches a new position and recalculates the electric field, which is affected by all imaginary charges in space. Therefore, to reduce calculation time, I select the same lattice division precision unit $h =0.1$mm the same as the Simultaneous over relaxation method to record every lattice potential. The potential distribution simulation are shown below in **Figure 3.2.2**.
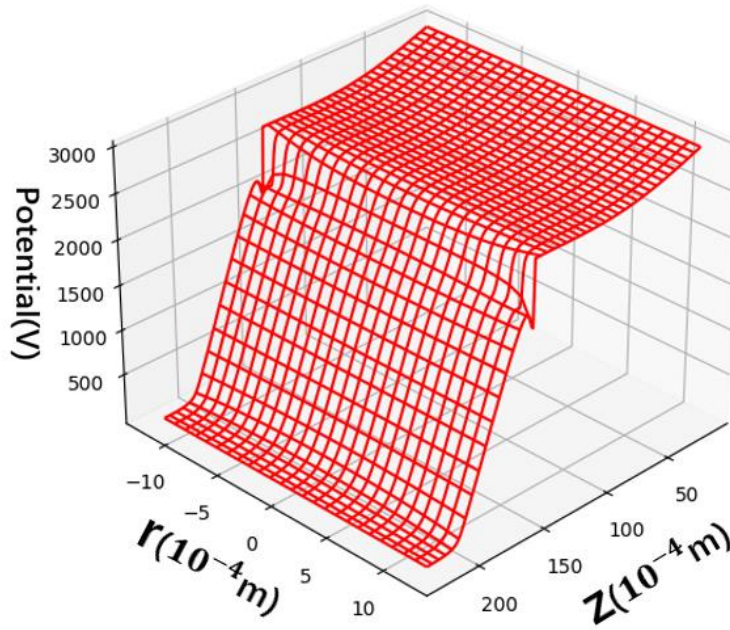
Relaxation method
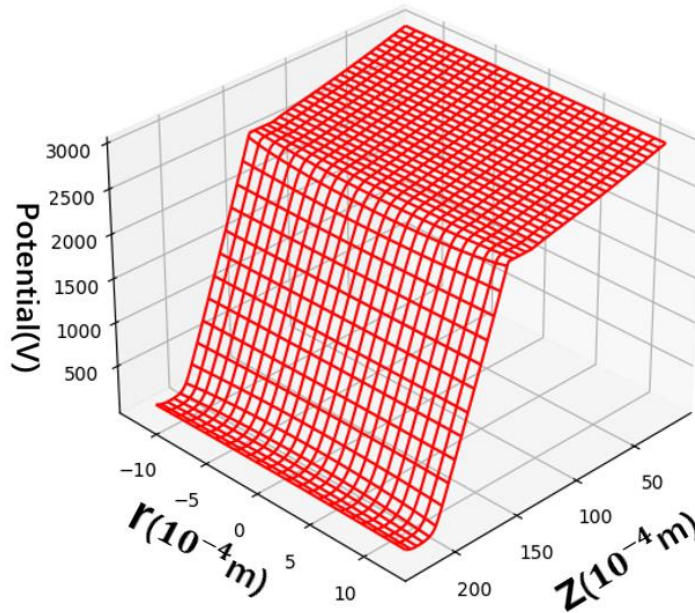
Surface charge method

Figure 3.2.2 – Potential distribution Diagram

Once the potential distribution at a lattice point is obtained, the corresponding lattice point electric field along the radial and z axes is calculated with an accuracy on the order of 2nd using the center-derivative method, as follows,

$$E_r(z, r) = \frac{\partial V(z, r)}{\partial r} = \frac{V(z, r+h) - V(z, r-h)}{2h}, \qquad (3.24)$$

$$E_z(z,r) = \frac{\partial V(z,r)}{\partial z} = \frac{V(z+h,r)-V(z-h,r)}{2h} . \qquad (3.25)$$

In the case of ions moving at random positions in the four lattice centers, the electric field $E(Z, R)$ can be calculated using this means as follows when the spatial potential and electric field are divided into a square lattice. A_1, A_2, A_3, and A_4 are the areas of the four blocks divided by the position of the ions, and a schematic diagram is shown in **Figure 3.2.3**

$$E(Z,R) = \frac{E_1(z+h,r)A_1+E_2(z+h,r)A_2+E_3(z+h,r)A_3+E_4(z+h,r)A_4}{A_1+A_2+A_3+A_4} \qquad (3.26)$$
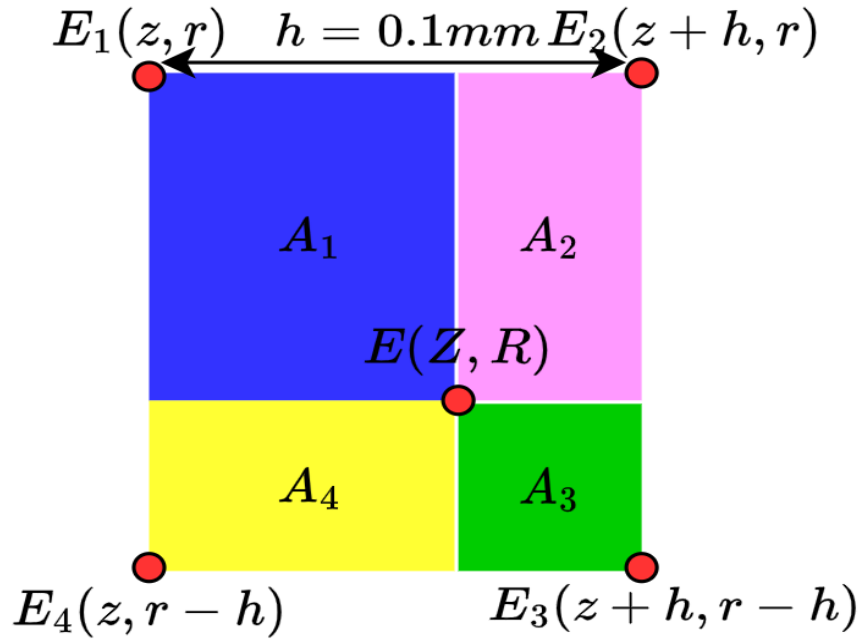

Figure 3.2.3.

3.2.2 Ion trajectory calculation and ray tracing

For an ion with already known mass m and charge q and electric field along r and z axis E_r and E_z, the equation of motion can be expressed as follows

$$m\frac{d^2r}{dt^2} = qE_r, \tag{3.27}$$

$$m\frac{d^2z}{dt^2} = qE_z, \tag{3.28}$$

By rewriting these equations as first-order ordinary differential equation of velocity with respect to time yields the following results.

$$\frac{dv_r}{dt} = \frac{q}{m}E_r, \tag{3.29}$$

$$\frac{dv_z}{dt} = \frac{q}{m}E_z. \tag{3.30}$$

To solve these ordinary differential equations with high accuracy, trajectory simulations were performed using the fourth-order Runge-Kutta method. Let $f(r, v_r, t)$ and $a(r, v_r, t)$ denote the relationship between the displacement and velocity of ions in the interval Dt, which can be expressed by

$$f(r, v_r, t) = v_r \tag{3.31}$$

$$a(r, v_r, t) = \frac{q}{m}E_r, \tag{3.32}$$

$$kf1 = f(r, v_r, t) \times \Delta t \tag{3.33}$$

$$ka1 = a(r, v_r, t) \times \Delta t \tag{3.34}$$

$$kf2 = f(r + \frac{kf1}{2}, v_r + \frac{ka1 \times \Delta t}{2}, t + \frac{\Delta t}{2}) \times \Delta t \tag{3.35}$$

$$ka2 = a(r + \frac{kf1}{2}, v_r + \frac{ka1 \times \Delta t}{2}, t + \frac{\Delta t}{2}) \times \Delta t \tag{3.36}$$

$$kf3 = f(r + \frac{kf2}{2}, v_r + \frac{ka2 \times \Delta t}{2}, t + \frac{\Delta t}{2}) \times \Delta t \tag{3.37}$$

$$ka3 = a(r + \frac{kf2}{2}, v_r + \frac{ka2 \times \Delta t}{2}, t + \frac{\Delta t}{2}) \times \Delta t \tag{3.38}$$

$$kf4 = f(r + \frac{kf3}{2}, v_r + \frac{ka3 \times \Delta t}{2}, t + \frac{\Delta t}{2}) \times \Delta t \tag{3.39}$$

$$ka4 = a(r + \frac{kf3}{2}, v_r + \frac{ka3 \times \Delta t}{2}, t + \frac{\Delta t}{2}) \times \Delta t \qquad (3.40)$$

So, the position and velocity of the ion along the radial axis after the time interval Δt can be determined by the weight ratio of the four results as follows.

$$v_r \left(t + \frac{\Delta t}{2}\right) = v_r(t) + \frac{ka1 + ka2 + ka3 + ka4}{6}, \qquad (3.41a)$$

$$r \left(t + \frac{\Delta t}{2}\right) = r(t) + \frac{kf1 + kf2 + kf3 + kf4}{6}. \qquad (3.41b)$$

The same calculation was performed for the z-axis direction to obtain the position and velocity of the ions, yielding the following equation.

$$v_z \left(t + \frac{\Delta t}{2}\right) = v_z(t) + \frac{ka1 + ka2 + ka3 + ka4}{6}, \qquad (3.42a)$$

$$z \left(t + \frac{\Delta t}{2}\right) = z(t) + \frac{kf1 + kf2 + kf3 + kf4}{6}. \qquad (3.42b)$$

3.2.3   Confirmation of simulation stability

The validity of the potential distribution simulation method introduced in Section 3.1 was investigated by comparing it with the ion trajectories obtained from the trajectory simulations presented in the previous section. For the surface charge method, as mentioned in the previous Section 3.1.1, the density and distribution of the contour points according to the structure affect the potential distribution between the electrodes. Therefore, the stability of the ion trajectories was observed while appropriately increasing or decreasing the number of contour points in important areas.
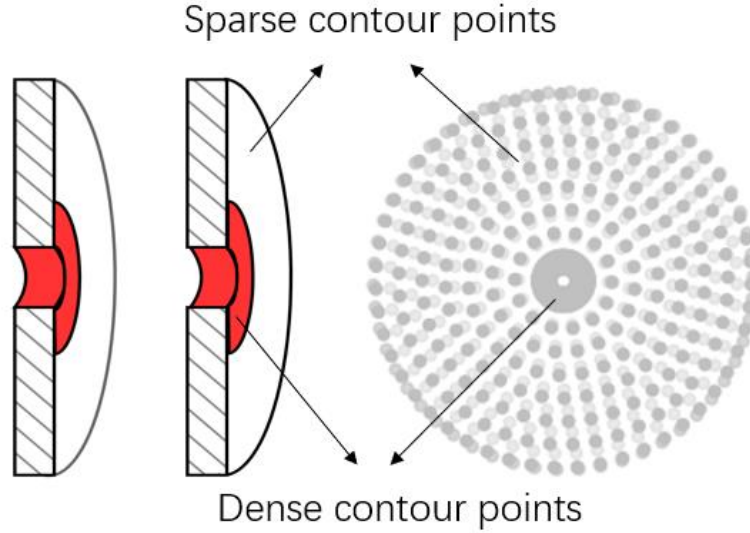
Figure 3.2.4 – Contour points distributed electrodes

As shown in **Figure 3.2.4**, on the left figure the red region due to being close to the ion path with large $f_1 = 0.8$, and the white region is far from the center of ion path with small $f_2 = 0.2$, right one is actual contour points. According to equation (3.4) keep both f_1 and f_2 keep constant while changing the length values a and b (the relationship between a and b is shown in **Figure 3.1.5**). The potentials are the same value as described in Section 3.2.1. i.e., $V_1 = 3000\ \text{V}, V_2 = 2700\ \text{V}, \text{MCP} = -1600\ \text{V}$. Monovalent ions of cesium (C_s^+) was used as test ion emitted from the center of the sample plate along the z axis velocity of 2000 m/s and the r axis velocity of 500 m/s to observe the trajectory. The selected values of a and b and the corresponding ion end positions and velocities are listed in Table 3.1, and the trajectories are shown in **Figure 3.2.5.**

Table 3.1: Values of a and b and the corresponding ion end positions and velocities

f_1	a(mm)	b(mm)	Contour points	r(mm)	v_z(m/s)	v_r(m/s)	Time of flight(μs)
method1	0.2	0.125	11243	-5.607	81244.718	-1872.419	4.2325
method2	0.32	0.2	8251	-5.562	81237.061	-1856.945	4.2305
method3	0.16	0.1	13991	-5.623	81235.563	-1877.398	4.2330
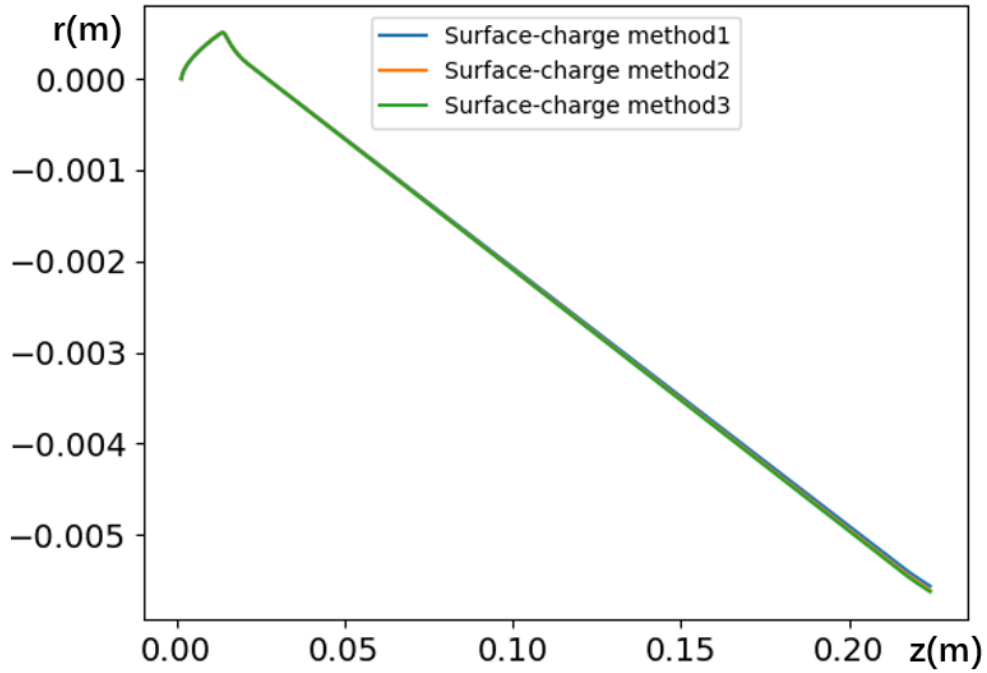
Figure 3.2.5 – Ion trajectories at various contour point-to-imaginary charge distances a and contour point-to-contour point distances b

To observe the stability of the ion's orbit, the contour points in the paraxial part are made larger or smaller. z axis difference Δz within 0.061 mm, and TOF difference Δt within 2.5 ns. The number of contour points of 11243 was selected for the subsequent simulation, and the imaginary charge distribution schematic is shown in **Figure 3.2.6.**
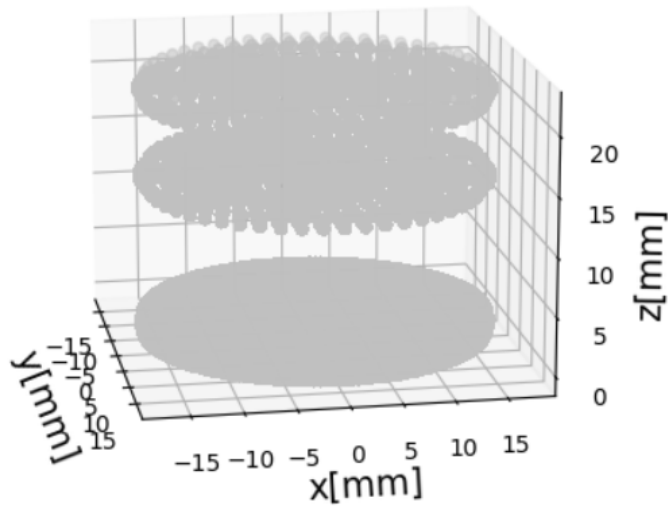
Figure 3.2.6.

3.2.4   Ion beam focusing test

Ions emitted from the sample plate at different angles of initial velocity can lead to divergence of the ion beam during its flight through the drift tube, resulting in a decrease in ion detection efficiency. Therefore, the relationship between the voltage of the two-stage acceleration electrode and the ion trajectory was investigated. The voltages of the sample plate V_1 and the first aperture V_2 (see **Figure 3.2.1)** was varied, and the changes in the focusing of the ion trajectory were observed the potential and trajectory simulations in the system were performed using the surface charge method and the Runge-Kutta method, and the C_s^+ is selected as example emitted from the sample plate with an initial velocity of 3000 m/s ($\sim$3.74eV) from -90 degrees to 90 degrees.
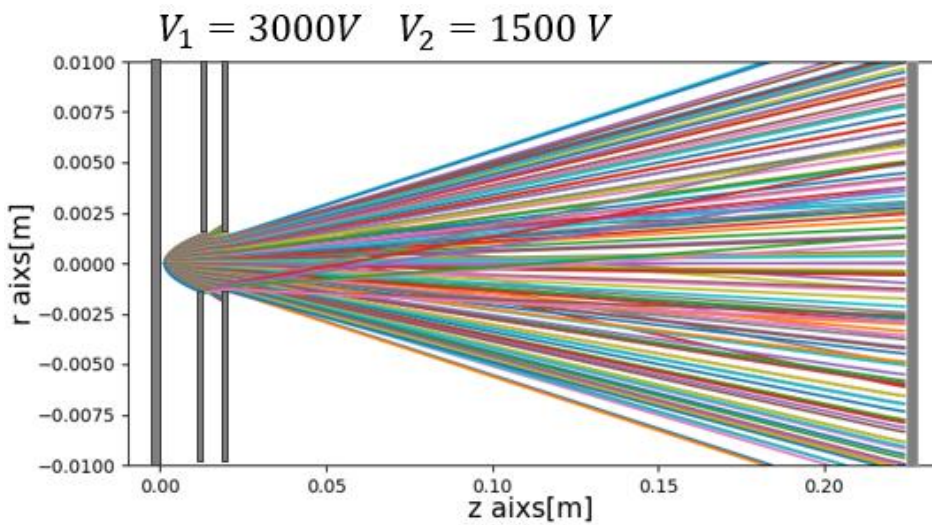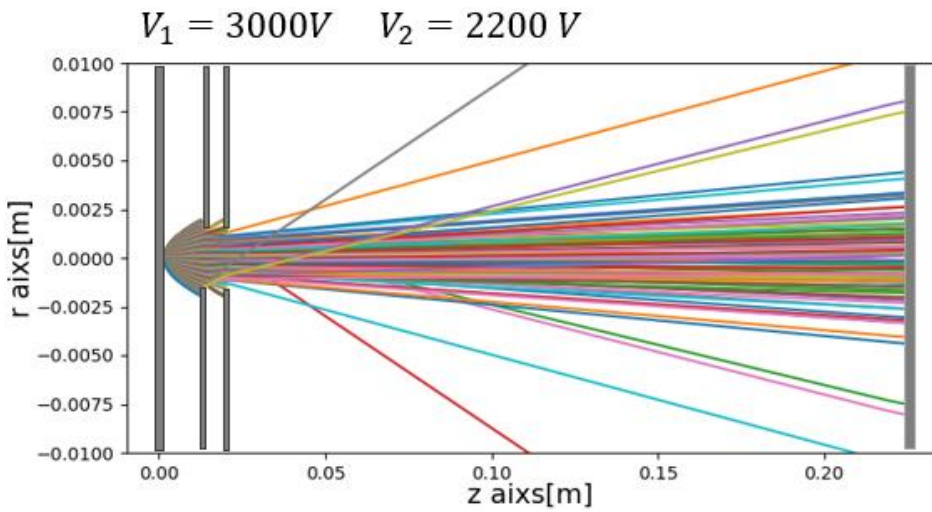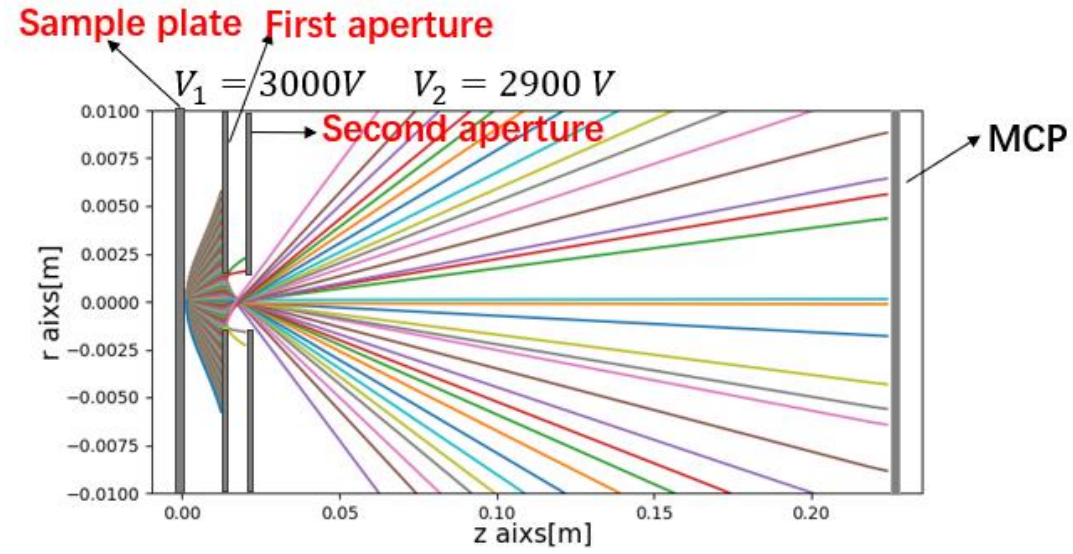
Figure 3.2.7 C_s^+ emission trajectories

At V_2=2900 V, most C_s^+ ions are blocked at the first aperture, defocusing in the drift path region, and only a few ions can finally reach the endpoint, detection efficiency is 0.06. At V_2=2200 V, the detection efficiency increased and the final ions were also focused to the MCP center, detection efficiency is 0.46. At V_2=1500V, detection efficiency increased to 0.57. The trajectories of C_s^+ ions at these voltages are shown corresponding to **Figures 3.2.7** a, b, and c, respectively. Thus, it was theoretically possible to optimize the detection signal by controlling the ion trajectory according to the appropriate potential distribution based on the actual initial velocity distribution of the ions. Later, we will analyze the initial velocity distribution of ions based on the relationship between the laser pulse and the ionization of ions.

3.3　Laser pulse control

This section describes the control of the laser pulse duration by group velocity dispersion compensation. [27] In the time domain, a coherent optical pulse electric field can be written in this form,

$$\varepsilon(t) = E(t)\cos\left[\omega_0 t + \phi(t)\right], \tag{3.43}$$

where $E(t)$ is the envelope amplitude, ω_0 is the carrier frequency and $\phi(t)$ is the temporal phase. Assuming the pulse shape to be Gaussian and using a complex expression, equation (3.43) becomes

$$\varepsilon(t) = E_0 e^{-2ln2\left(\frac{t}{\tau}\right)^2} e^{i[\omega_0 t + \phi(t)]}, \tag{3.44}$$

where τ determines the minimum pulse duration, $\phi(t)$ determines the temporal relationship between the frequency components and plays a vital role in controlling the pulse duration. In the time domain form, it is intuitive to understand the pulse shape, but in utilization, we have to change to the frequency domain to calculate material dispersion.

$$\varepsilon(\omega) = U_0 e^{-2ln2\left(\frac{\omega-\omega_0}{\Delta\omega}\right)^2} e^{i\varphi(\omega)}, \tag{3.45}$$

where $U_0 e^{-2ln2\left(\frac{\omega-\omega_0}{\Delta\omega}\right)^2}$ is the spectral amplitude part and $\varphi(\omega)$ is the spectral phase. The spectral phase is described when the pulse propagates through a dispersive material

$$\varphi(\omega) = -\beta(\omega)L. \tag{3.46}$$

where L is the length in the dispersive material, $\beta(\omega)$ is the propagation constant. By expressing the spectral phase as a Taylor expansion around carrier frequency ω_0 follows

$$\beta(\omega) = \beta(\omega_0) + \frac{d\beta}{d\omega}\bigg|_{\omega_0}(\omega-\omega_0) + \frac{1}{2}\frac{d^2\beta}{d\omega^2}\bigg|_{\omega_0}(\omega-\omega_0)^2 \tag{3.47}$$

$$+ \sum_{m=3}^{\infty}\frac{1}{m!}\frac{d^m\beta}{d\omega^m}\bigg|_{\omega_0}(\omega-\omega_0)^m + \cdots.$$

The first term of equation (3.47) is related to the phase delay of the carrier, and the phase velocity can be written as

$$v_p = \frac{n_I(\omega)}{c} = \frac{\beta(\omega_0)}{\omega_0}, \tag{3.48}$$

where $n_I(\omega)$ is the material imaginary part of the complex refractive index of a material. The second term is related to the group velocity v_g of laser pulse and can change the delay of the pulse envelope as,

$$v_g = \frac{1}{\frac{d\beta}{d\omega}\big|_{\omega_0}}.$$
(3.49)

The third term is related to the pulse width and called group velocity dispersion (GVD), can be expressed as

$$GVD = \frac{d^2\beta}{d\omega^2}\bigg|_{\omega_0} = \frac{d}{d\omega}\left(\frac{1}{v_g}\right)$$
(3.50)

$$= -\frac{1}{v_g^2(\omega_0)}\frac{dv_g}{d\omega},$$

the unit of GVD is $[fs^2/mm]$. The definition of (group delay dispersion) GDD $[fs^2]$ is

$$GDD = \frac{d^2\varphi}{d\omega^2}\bigg|_{\omega_0}$$
(3.51)

Therefore, this formula can be used to calculate the GDD in different dispersive materials by using equation (3.46) and (3.51)

$$GDD = GVD \cdot L.$$
(3.52)

Generally, the higher order of phase expansion parts can be neglected, just for the narrow spectrum or few-cycle near-infrared laser (NIR) lasers case the high order parts should be concerned. Using the Fourier transform, the relation between the duration of the output laser pulse duration τ_{out} and input laser pulse duration τ_{in} is [21]

$$\tau_{out} = \tau_{in}\sqrt{1 + (4\,ln\,2\,\frac{GDD}{\tau_{in}^2})^2}$$
(3.53)

Reflections and transmissions at many optical mirrors and lenses add positive compensation to the GDD, which causes the pulse width to widen. Therefore, negative GDD compensation is needed to recompress the pulse width.

For negative GDD compensation in ultrafast optics, slab, prism pairs, or gratings can be used [21]. In the following, I introduce the theoretical calculation of prism pairs and the compensation mechanism used in this experimental system.
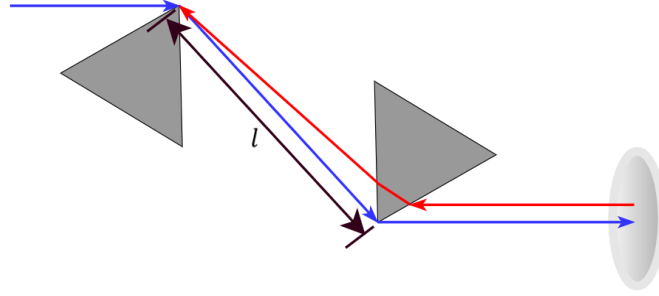
Figure 3.3.1 – Double pass Prism pairs configuration

The group velocity dispersion compensation by prism pair consists of two prisms. The first prism disperses the beam to generate a path length difference, giving negative dispersion. Denoting this dispersion as $GDD_{negative}$, it can be written as

$$GDD_{negative} = -\frac{d^2\varphi}{d\omega^2} = -l\frac{\lambda^3}{2\pi c^2}\left(\frac{d\theta}{d\lambda}\right)^2, \qquad (3.53)$$

where λ is the center wavelength of laser, l is the distance between two prism apexes as shown in **Figure 3.3.1**. When the laser incident angles of the prism pairs satisfy the Brewster angle, the reflection loss can be minimized, and the $GDD_{negative}$ can be written as

$$GDD_{negative} = -l\frac{\lambda^3}{2\pi c^2}\left(\frac{d\theta}{d\lambda}\right)^2 \approx -4l\frac{\lambda^3}{2\pi c^2}\left(\frac{dn}{d\lambda}\Big|_{\lambda_0}\right)^2 \qquad (3.54)$$

The second prism only collimates the laser beam and does not contribute to $GDD_{negative}$. The following Sellier equation can be used to calculate $(dn/d\lambda)|_{\lambda_0}$ in Equation (3.55),

$$n^2(\lambda) = 1 + \frac{B_1\lambda^2}{\lambda^2-C_1} + \frac{B_2\lambda^2}{\lambda^2-C_2} + \frac{B_3\lambda^2}{\lambda^2-C_3} \qquad (3.55)$$

where B_1, C_1, etc. are material parameters and are available from online optical databases such as [28].
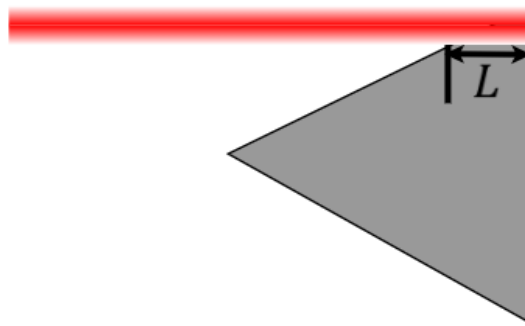

Figure 3.3.2 – laser beam diameter in prism material

The positive group delay dispersion $GDD_{positive}$ is directly caused by the prism material itself. Since the laser beam diameter is not negligible in prism, and the pass length L should be considered, as **Figure 3.3.2**, Considering the group velocity dispersion of the prism material and the laser transit length L, $GDD_{positive}$ can be easily calculated using Equation (3.52),

$$GDD_{positive} = GVD_{prism} \cdot L,$$

The prism pair used in this study is placed in a double-pass configuration, as shown in **Figure 3.3.1**, where the laser light passes through the prism pair, is reflected by a mirror, and then passes through the prism pair again. Therefore, the GDD of the entire prism pair is considered to be doubled. Substituting equations (3.54) and (3.52) into equation (3.53), the relationship between the pulse widths and the prism pair is expressed as follows.

$$\tau_{out} = \tau_{in}\sqrt{1 + (4ln2\frac{GDD_{prism}}{\tau_{in}^2})^2}$$

$$= \tau_{in}\sqrt{1 + (4ln2\frac{2GDD_{negative} + 2GDD_{positve}}{\tau_{in}^2})^2}$$

$$= \tau_{in}\sqrt{1 + (8ln2\frac{-4l\frac{\lambda^3}{2\pi c^2}(\frac{dn}{d\lambda}\big|_{\lambda_0})^2 + GVD_{prism} \cdot L}{\tau_{in}^2})^2}$$

From this equation, it can be seen that all parameters other than L and l are known and fixed. Therefore, pulse width control can be achieved by designing an appropriate optical path to control L and l.

3.4   Femtosecond laser induced initial velocity distribution

In laser ionization, which takes place on femtosecond time scales, the interaction between photons and electrons dominates the entire process, including the absorption of laser energy by electrons, energy transfer between electrons and the lattice, and plasma formation and expansion. Therefore, a relatively appropriate model, corresponding to the actual experimental situation, was introduced to simulate the dynamics of laser-induced ion emission. The model is based on the Maxwell-Boltzmann velocity distribution model of particle and takes into account the expansion effect of the surface plasma and the accelerating electric field effect due to high-energy surface electrons, and the kinetic energy distribution of the ions is expressed as (3.56) using two shifted velocities. [18].

$$F(v_z) = (m/2\pi k_B T)^{\frac{3}{2}} v_z^3 \exp\left[-\frac{m}{2k_B T}(v_z - v_k - v_c)^2\right] \qquad (3.56)$$

where v_z is the plasma expansion velocity and v_c is called coulomb velocity caused by the strong electric field formed by highly energetic electrons which gather above the sample surface. These two velocities are expressed as

$$v_k = \sqrt{\frac{\gamma k_B T}{m}}, \qquad\qquad\qquad\qquad (3.57)$$

$$v_c = \sqrt{\frac{2ezV_0}{m}} \qquad\qquad\qquad\qquad (3.58)$$

Here $\gamma = 5/3$ is the adiabatic coefficient, the value is the same in all directions of emission of ions. The electric field is directly affected by the energy and density of the electrons, and when the electric field force is large enough it will drag the cold ions from the target surface without heat transfer between the energetic electron and lattice. A schematic diagram of this situation is shown in **Figure 3.4.1**. The velocity v_c direction is always perpendicular to the linear dependence of the target with the ion charge state z. V_0 is the equivalent steady-state voltage produced by electrons in the plasma after femtosecond laser irradiation.
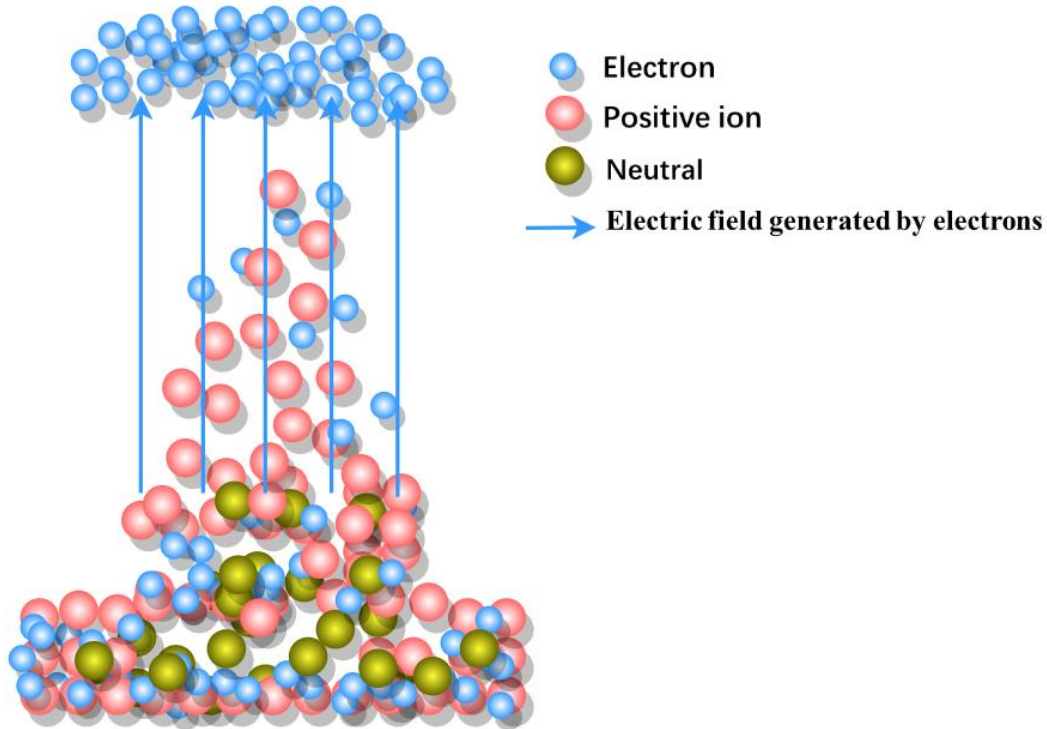
Figure 3.4.1 – Schematic of laser-surface interactions

For the femtosecond level ion kinetic energy distribution, the plasma expansion process is small and negligible compared to the overall shifted velocity because the laser directly transfers the entire energy to the electrons before the electron-lattice heat transfer and the bulk of plasma generation. Considering the actual situation, the mass spectrum of different charge states for the same ion cannot be observed temporarily in our experiment, therefore it is hard to estimate the effect of the Coulomb velocity term and distinguish v_k or v_c which term dominates the whole shift velocity in (3.56). In that case, I changed the shifted-MB distribution to this form by combing v_k and v_c terms to one v_{shifted} term, and considered the shifted velocity as a whole. The velocity distribution is shown in **Figure 3.4.2.**
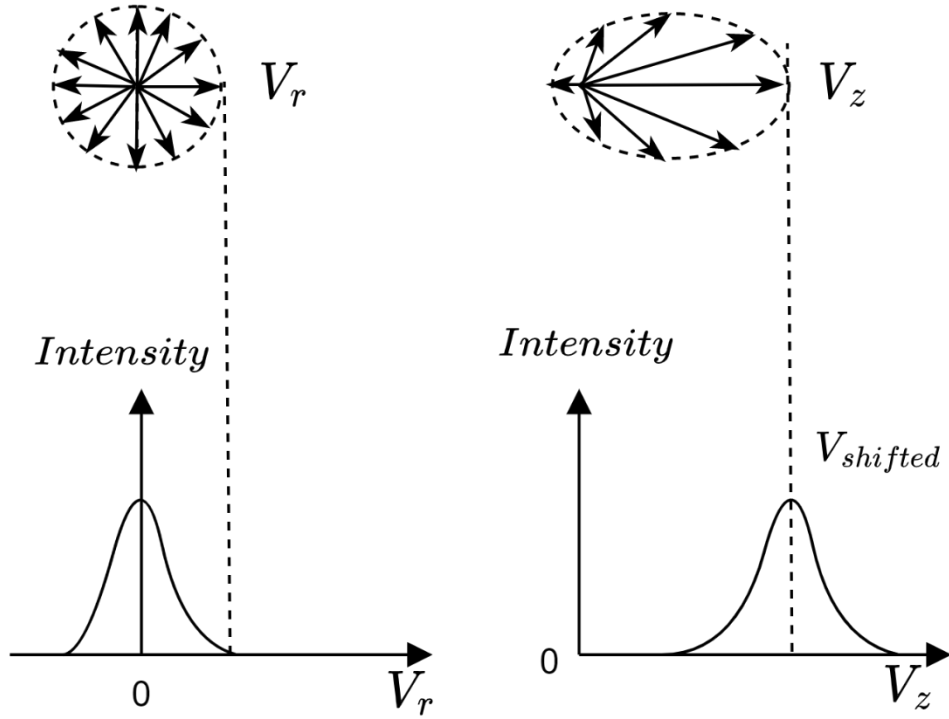
Figure 3.4.2 –Initial velocity distribution along the r-axis and z-axis

Consider the shifted velocity as a whole, along the target normal v_z expressed as

$$f(v_z) = (m/2\pi k_B T)^{\frac{1}{2}} \exp\left[-\frac{m}{2k_B T}(v_z - v_{\text{shifted}})^2\right] \qquad (3.59)$$

The velocity distribution on the r axis is not perpendicular to the sample plate expressed as

$$f(v_r) = (m/2\pi k_B T)^{\frac{1}{2}} \exp\left[-\frac{m}{2k_B T}(v_r)^2\right] \qquad (3.60)$$

Therefore, if T and v_{shifted} confirmed, the initial velocity distribution of ion can be determined along the z axis and r axis respectively. Additionally, the TOF difference can be calculated by simulating the ions' trajectory in the system by using the initial velocity distribution $f(v_z)$ and $f(v_r)$, and the maximum TOF difference can be assumed to signal width and time resolution.

3.5   Deriving initial velocity distribution from experimental data

After obtaining the experimental mass spectrum, how to derive the corresponding ion's initial velocity distribution depends on the signal intensity distribution. First, we should determine a rough range of velocities $\{v_1, v_2, \cdots, v_n\}$ **Figure 3.5.1**

Figure 3.5.1 –Different vectors of velocities

These are the vectors of velocities that we want to figure out. Next, we write an initial density distribution as p:

$$\begin{pmatrix} p_1 \\ p_2 \\ \vdots \\ p_n \end{pmatrix}$$

and the $p_j (j = 1, \cdots, N)$ directly corresponds to the ratio of the ion's initial velocity v_j. For the ion's experiment signal s_{exp}, based on the sampling interval Δt set by the oscilloscope, we can divide s_{exp} into T equal interval of the signal width t_{width} divided by the Δt

$$T = \frac{t_{width}}{\Delta t} \tag{3.61}$$

Then, set the initial velocities of the ions and let them through the system trajectory simulation. Therefore, we can get each ion arrival time and corresponding to the initial velocity.

$$\begin{pmatrix} v_1 \\ v_2 \\ \vdots \\ v_n \end{pmatrix} \xRightarrow{\textit{Trajectory Simulation}} \begin{pmatrix} t_1 \\ t_2 \\ \vdots \\ t_n \end{pmatrix}.$$

For the set of arriving time $\{t_1, t_2, \cdots, t_n\}$ we also need to write t_j as $t_j = i\Delta t$ form, and $i(1 < i \leq T)$. After that we define a $T \times N$ matrix $f = \{f_{ij}\}$ as follows:

$$f_{ij} = \begin{cases} 1 & (t_j = i\Delta t) \\ 0 & (other) \end{cases}. \tag{3.62}$$

With f and p we can calculate the simulated signal

$$s_{sim} = fp, \tag{3.63}$$

In order to make the s_{sim} shape better fit the s_{exp} shape, we have to adjust p to achieve data fitting, therefore the least squares method is employed and defined the cost function F as

$$F = |s_{sim} - s_{exp}|^2 \tag{3.64}$$

$$= |fp - s_{exp}|^2$$

$$= \sum_{i=1}^{T} [\sum_{j=1}^{N} f_{ij} p_j - s_i^{exp}]^2.$$

To minimize F, we set $\partial F / \partial p_j = 0$ $(j = 1, \cdots, N)$ and we can get

$$\frac{\partial F}{\partial p_j} = \sum_{i=1}^{T} 2f_{ij} \left[\sum_{k=1}^{N} f_{ik} p_j - s_i^{exp} \right] = 0, \tag{3.65}$$

and transform it to get the next expression

$$\sum_{k=1}^{T} (\sum_{i=1}^{N} f_{ik} f_{ij}) p_k = \sum_{k=1}^{T} s_i^{exp} f_{ij}, \tag{3.66}$$

Finally, define $N \times N$ matrix $A = \{f_{jk}\}$ and N-dimensional vector $b = \{b_j\}$ and express as:

$$A_{jk=} \sum_{i=1}^{N} f_{ik} f_{ij}, \tag{3.67}$$

$$b_j = \sum_{k=1}^{T} s_i^{exp} f_{ij}. \qquad (3.68)$$

By using

$$Ap = b, \qquad (3.69)$$

Finally, we can figure out the initial velocity $\{v_1, v_2, \cdots, v_n\}$ corresponding distribution ratio $p_j (j = 1, \cdots, N)$ by combing experiment signals shape and simulation of the trajectory.

3.6 How to use the analysis method

In this chapter, the initial velocity distribution simulation of ions and the trajectory tracing when ions enter the acceleration electric field; the final signal analysis and the corresponding relationship between the velocity distribution and the signal are discussed. On how to reasonably combine and utilize these three parts of simulation for ions emission, trajectory tracing, and detection to achieve the most suitable signal analysis and ion velocity observation. The idea at this stage is to determine the ion temperature T and v_{shifted} through the detected signal width τ_{signal}, since a signal is constituted by continuous time interval as shown in **Figure 3.6.1**.
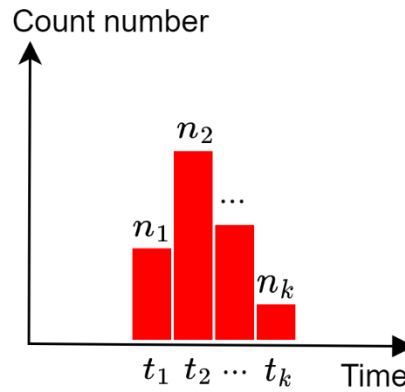

Figure 3.6.1

for the signal width τ_{signal}, it depends on whether the beginning of the signal and the end of the signal time interval count number n and this overall count number $n_1 + n_2 + \cdots + n_k$ satisfy the condition:

$$\frac{n_k}{n_1 + n_2 + \cdots + n_k} \geq \frac{1}{100}, \tag{3.70}$$

where the corresponding time interval can be taken into account within the signal width

$$t_k - t_1 = \tau_{signal}, \tag{3.71}$$

The specific steps are to use the shifted-MB distribution with different temperatures T_i and different v_{shifted_j} to decide initial velocity distribution of emitted ions along z and r axis,

$$f(v_z) = (m/2\pi k_B T_i)^{\frac{1}{2}} \exp\left[-\frac{m}{2k_B T_i}(v_z - v_{\text{shifted}_j})^2\right],$$

$$f(v_r) = (m/2\pi k_B T_i)^{\frac{1}{2}} \exp\left[-\frac{m}{2k_B T_i}(v_r)^2\right]$$

and then let 100 ions enter the TOF system and do trajectory tracing with correspond $(T_i, v_{\text{shifted}_j})$ initial velocity distribution. Within 100 ions, when the TOF difference between the fastest ion t_f and the slowest ion t_s is equal to the signal width τ_{signal}, the ion emission temperature T_i and v_{shifted_j} can be determined.

$$t_s - t_f = \tau_{signal}$$

After the initial velocity distribution is confirmed, then based on the distribution and set a specific velocity range $\{v_1, v_2, \cdots, v_n\}$ in the distribution region $(T_i, v_{\text{shifted}_j})$ and use least square method to figure out the velocity proportion of the intensity of the detected signal.

4 Observation of the initial velocity distribution by analyzing detected signals

INTRODUCTION

This chapter introduced the data analysis and simulation utilization based on the simulation methods mentioned in Chapter 3. The experiments were performed in a two-acceleration region linear mass spectrometer in this chapter, and the electrodes voltage setting will follow the voltage mark in **Figure 4.1** below.
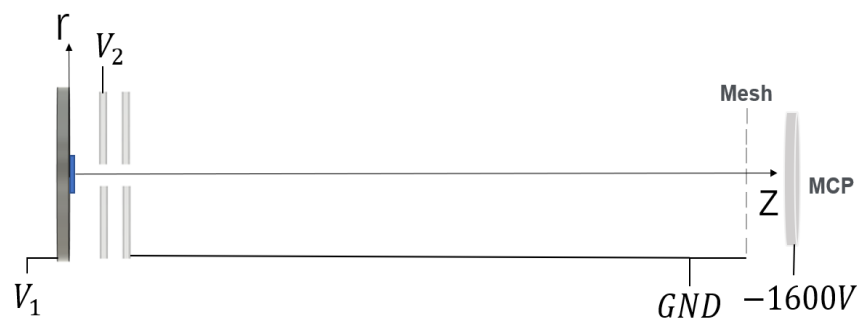

Figure 4.1 – The voltage applied to the system

The following experiments are conducted separately in this chapter:

(1) Three different positive ions of the mixed sample of CsI, KI, and NaI under different femtosecond laser intensity. After obtaining the TOF spectra of Cs^+, Na^+, K^+ , comparisons and calibrations will be made simultaneously. On the basis of aforementioned shifted-Maxwell Boltzmann (MB) distribution model and analytical method in Chapter 3, the ion bunch temperature T_i and the shifted velocity $v_{shifted}$ of each ion can be estimated by the width of the signal. Since there are different combinations of T_i and $v_{shifted}$ in shifted-MB distribution model that satisfy the signal width limitation, but only three ions simultaneously meet the same time calibration request can be selected to represent the ion temperature and shifted velocity.

(2) For the comparative study of femtosecond and nanosecond laser, we employed a 160 fs Ti: sapphire laser pulse with 800 nm wavelength and a 1 ns Nd: YAG third harmonic laser pulse with the same pulse energy of 2.5 μJ, and used CsI as the sample achieved the

observation of velocity distribution of Cs^+, and the generation of $(CsI)_n Cs^+$ ion clusters under different laser pulse durations.

(3) To explore femtosecond laser intensity dependence of the initial velocity distribution, we controlled the laser intensity to observe the ion temperatures and $v_{shifted}$ of Cs^+ near the ionization threshold of the sample CsI.

4.1 Cs^+, Na^+, K^+ signal detection and temperature, $\nu_{shifted}$ estimation

The voltage mark of the system is shown in **Figure 4.1**, $V_1 = 3000$V, first aperture $V_2 = 2700$V, MCP $= -1600$V, and the second aperture and mesh are GND. The experimental conditions are shown in Table 4.1.1.

Table 4.1.1: Experimental conditions

Sample	CsI, KI, NaI mixed
Pulse duration	160 fs
Laser frequency	10 kHz
Pulse energy	2.5/3.0/3.5/4.0 μJ
Sampling frequency	100 MHz

The TOF spectra of Cs^+, Na^+, K^+ with different pulse energy are shown in **Figure 4.2.**
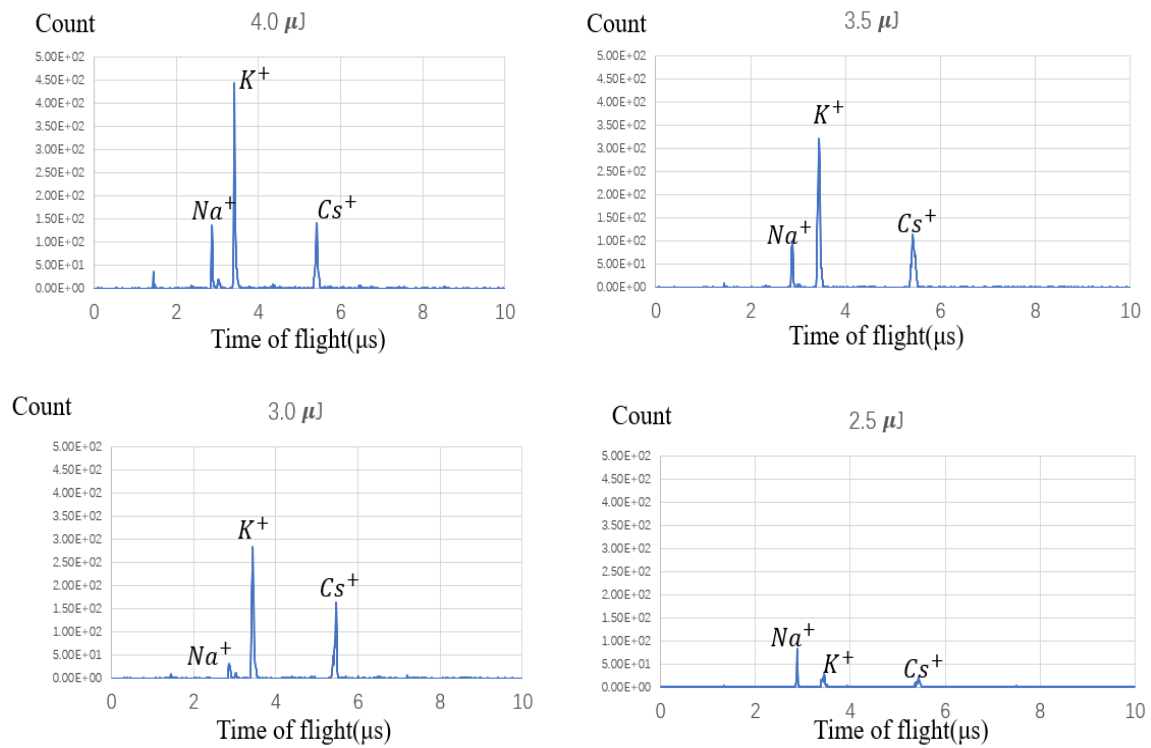
Figure 4.2 TOF spectra of Cs^+, Na^+, K^+

The width of the signal for each ion at each pulse energy is decided by equation (3.71) and shown in the Table 4.1.2.

Table 4.1.2: Signal width of Cs^+, Na^+, K^+ in different pulse energy

	2.5μJ	3.0μJ	3.5μJ	4.0μJ
C_s^+	0.13μs	0.13μs	0.15μs	0.11μs
K^+	0.11μs	0.13μs	0.12μs	0.10μs
N_a^+	0.04μs	0.07μs	0.08μs	0.06μs

The initial velocity distributions of desorbed ions were simulated following shifted-MB distributions model at different temperatures T_i and velocities v_{shifted_j}. The range of T_i was set from 0 K to 10^5 K with a calculation interval of 1000 K. The range of v_{shifted_j} was set from 0 m/s to 2×10^5 m/s with calculations performed every 1000 m/s. The number of ions emitted per simulation is 100, and the fitting results are shown in Table 4.1.3 below

Table 4.1.3 fitting (Temperature,v_{shifted})

$(T[K], v_{shifted}[m/s])$	2.5μJ	3.0μJ	3.5μJ	4.0μJ
C_s^+	(13000,4000)	(13000,4000)	(19000,5000)	(27000,4000)
K^+	(23000,12000)	(23000,30000)	(26000,12000)	(27000,16000)
N_a^+	(10000,37000)	(17000,31000)	(375000,30000)	(43000,33000)

The calibration time $t_{\text{original}} = 1.32$ μs was estimated by Cs^+, Na^+, K^+ simultaneously. The ion temperature T decreased as the pulse energy from 4.0μJ to 2.5μJ, and the v_{shifted} also decreased as the pulse energy decreases.

4.2 Cs^+ and CsI ion clusters spectra observation under nanosecond laser and femtosecond laser

In this section, for the comparative study of femtosecond and nanosecond lasers, we employed a 160 fs Ti: sapphire laser pulse with 800 nm wavelength and a 1.0 ns Nd: YAG third harmonic laser pulse. For the sample preparation in this part. a vacuum deposition apparatus was used to prepare the CsI deposition sample. The CsI powder was put into a crucible in the deposition apparatus with a spatula, heated to vaporize, and solidified on a thin stainless-steel plate. The temperature of the crucible was adjusted to 2 Å/s with a slidac. The deposition was carried out for 5 hours to a thickness of approximately 1 μm.

4.2.1   Nanosecond laser

The nanosecond laser was used to observe the initial velocity distribution and temperature of Cs^+. The parameters of the nanosecond laser source and sample are shown in Table 4.2.1.

Table 4.2.1: nanosecond Laser parameters

Sample	CsI
Laser Pulse duration	1 ns
Laser frequency	200 Hz
Pulse energy	2.5 μJ

The voltage setting of the experiment is shown in **Figure 4.1.** The target voltage was held to a potential of V_1 =1.5kV,2.0kV,2.5kV and 3.0kV separately, V_2 =0V. The TOF spectra of Cs^+ and $(CsI)_n Cs^+$ are shown in **Figure 4.3**.
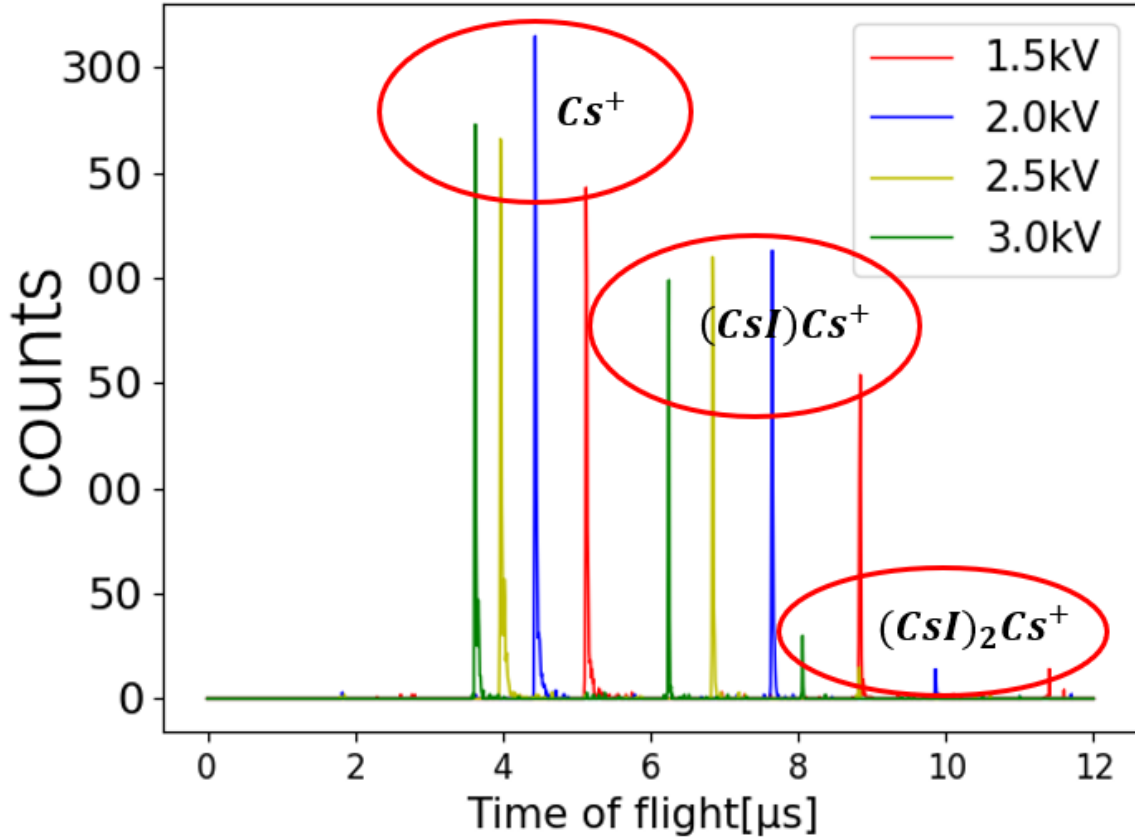
Figure 4.3 TOF spectra of Cs^+ and $(CsI)_n Cs^+$ under nanosecond laser

The shifted-MB distribution model has been used to simulate the initial velocity of laser induced ions. Select Cs^+ as the simulation ion to emit 100 particles into the system and proceed trajectory simulation, the range of T_i was set from 0 K to 100000 K with a calculation interval of 1000 K. The equations for the initial velocity distribution along the z and r axes were determined by Equations (3.59) and (3.60), the signal width was decided by equation (3.71). By the statistics of **Figure 4.3** signal width of Cs^+ in different voltages, and compiled in Table 4.2.2.

Table 4.2.2.

Sample plate voltage	1.5kV	2.0kV	2.5kV	3.0kV
$\tau_{signal}(Cs^+)$	$0.12\mu s$	$0.10\mu s$	$0.11\mu s$	$0.08\mu s$

After knowing the signal width τ_{signal}, by fitting the ion temperature and $v_{shifted}$ based on the aforementioned analytical method in chapter 3 conclusion part, the Cs^+ estimation temperature was about $0.6 \times 10^5 K \sim 0.7 \times 10^5 K$, $v_{shifted}$ was 3.5 km s^{-1}~4.5 km s^{-1}. At the same laser pulse energy, this result shows larger values than the previously reported initial velocity 1.3 km s^{-1} [29] for the mean velocity of Cs^+, but the temperature prediction agrees with about $10^5 K$ [30]. The calibration time was $t_{original} = 0$ μs (error range can be controlled within 0.28%). Based on the $t_{original}$ and estimation velocity range, and just considering the velocity along the normal to the target surface, the signal interval corresponding to the sample plate voltage was held to different potentials can be observed in **Figure 4.4.** Within a 6% error range between simulation and actual observation, as the V_1 gradually increased, the initial velocity derived from the signal also increases, and the velocity distribution also shifted to the direction of higher velocity.
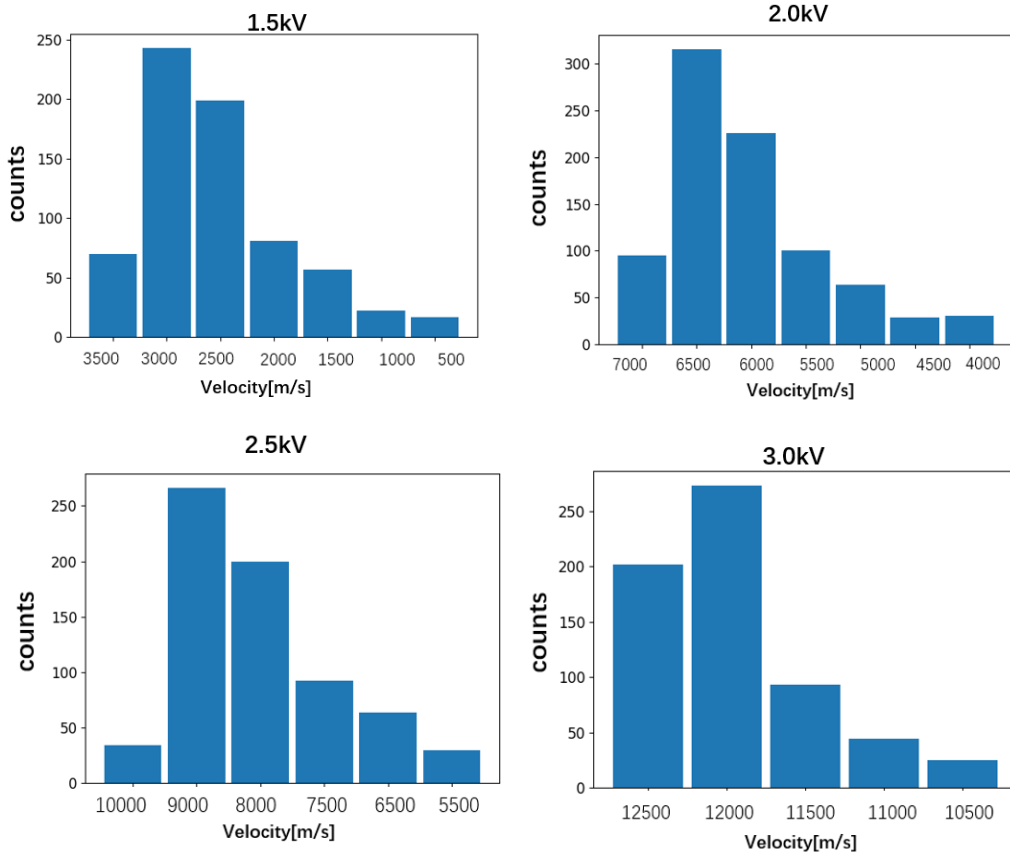

Figure 4.4

65

4.2.2 Femtosecond laser

Using femtosecond laser pulse of the same pulse energy to observe the initial velocity distribution and temperature of Cs^+. The parameters of the femtosecond laser are shown in Table 4.2.3.

Table 4.2.3: femtosecond laser parameters

Sample	CsI
Pulse duration	160 fs
Laser frequency	10 kHz
Pulse energy	2.5 μJ
Sampling frequency	100 MHz

The TOF spectra of Cs^+ and $(CsI)_n Cs^+$ are shown in **Figure 4.5**.
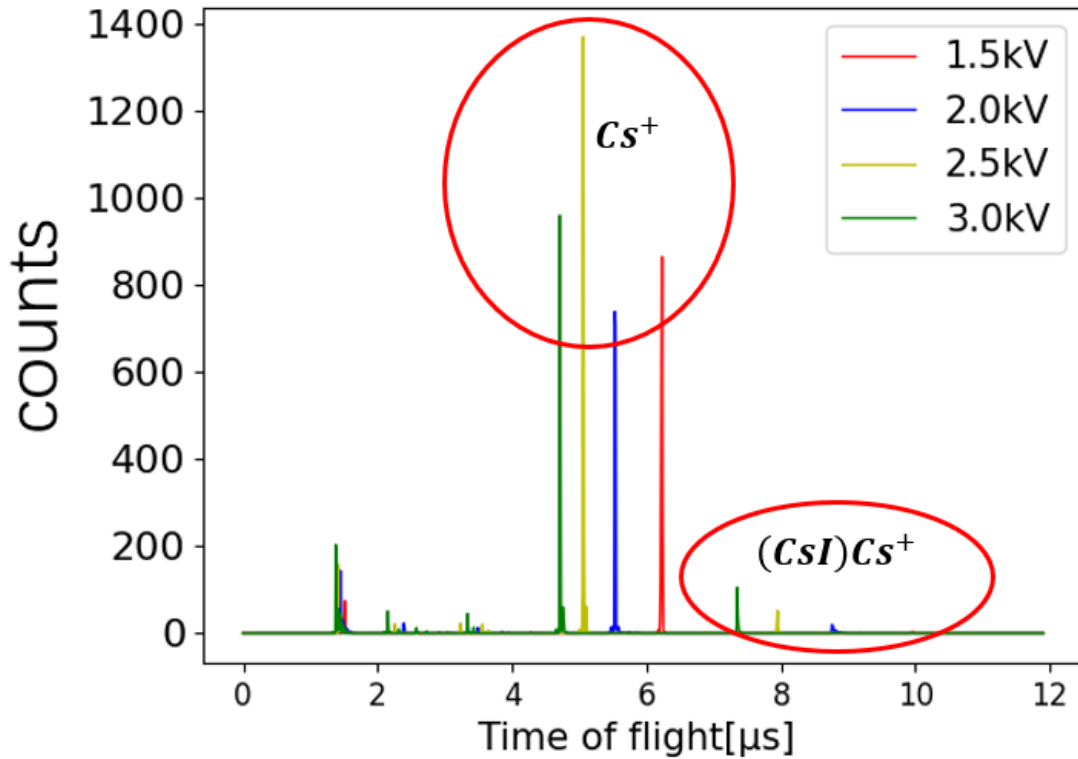
Figure 4.5 TOF spectra of Cs^+ and $(CsI)_n Cs^+$ under femtosecond laser

By the statistics of **Figure 4.5** signal width of Cs^+ in different voltages, and compiled in Table 4.2.4.

Table 4.2.4

Sample plate voltage	1.5kV	2.0kV	2.5kV	3.0kV
τ_{signal}	$0.05\mu s$	$0.04\mu s$	$0.03\mu s$	$0.02\mu s$

According to the fitting under different ion temperature T and velocity $v_{shifted}$ terms, the Cs^+ under 2.5μJ fs laser pulse temperature range was 5000K~7000K, $v_{shifted}$ range was 4.0 km s^{-1}~12.0 km s^{-1}, the calibration time was $t_{original} = 1.32$ μs. Based on the $t_{original}$ and estimation velocity range, as the **Figure 4.6** shown, as the V_1 gradually increased, the initial velocity derived from the signal also increases, and the velocity distribution also shifted to the direction of higher velocity.
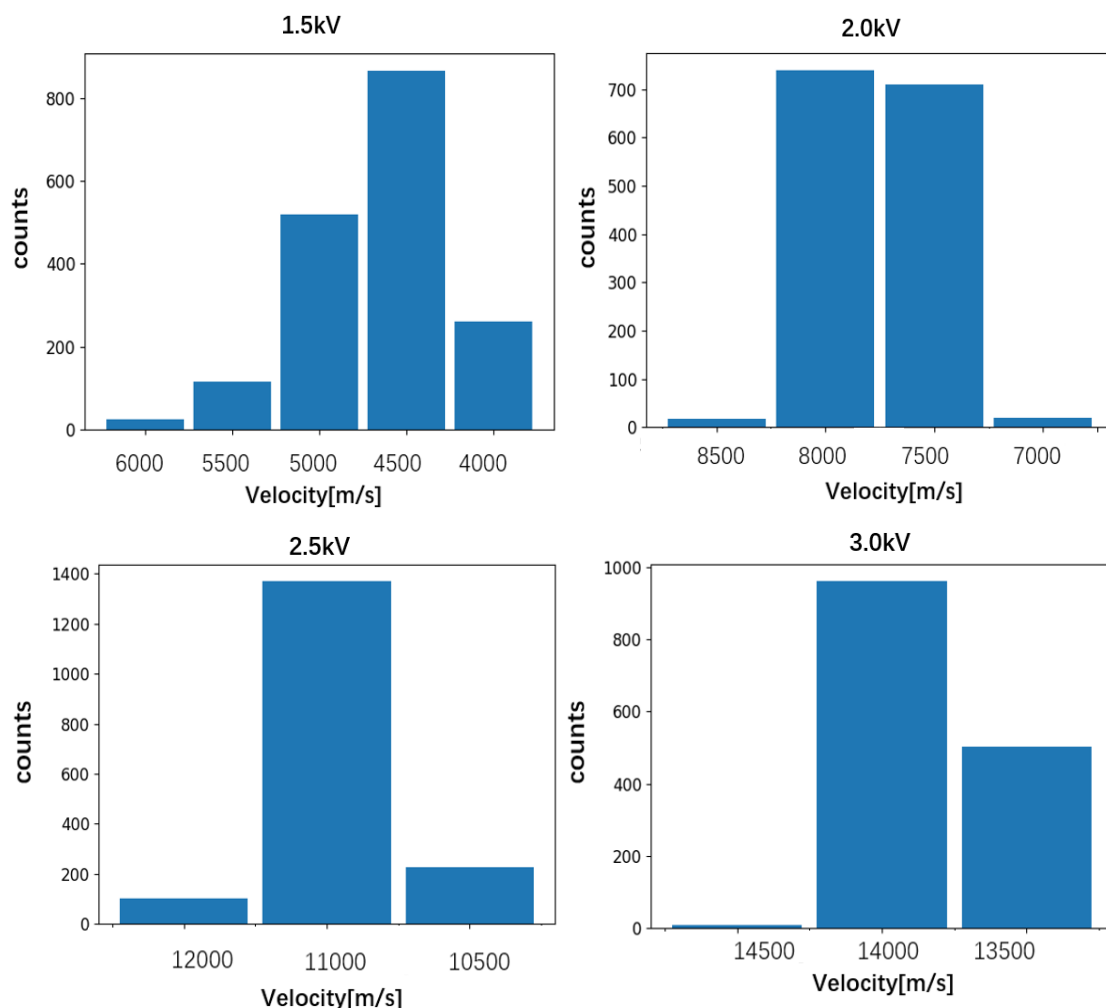
Figure 4.6

4.2.3 Comparison of femtosecond and nanosecond laser results

The group data of the femtosecond laser and the nanosecond laser with the sample plate voltage of 3kV were selected for comparison. Since the section 4.2.1 and 4.2.2 already estimated the $t_{original}$ and Cs^+ velocity under nanosecond and femtosecond laser separately. The calibrated TOF spectra of Cs^+ and CsI clusters is shown in **Figure 4.7.** In the femtosecond laser case, Cs^+, $(CsI)Cs^+$ can be detected, and Cs^+ with high signal intensity. For the nanosecond laser case, Cs^+, $(CsI)Cs^+$ and $(CsI)_2Cs^+$ can be simultaneously detected.
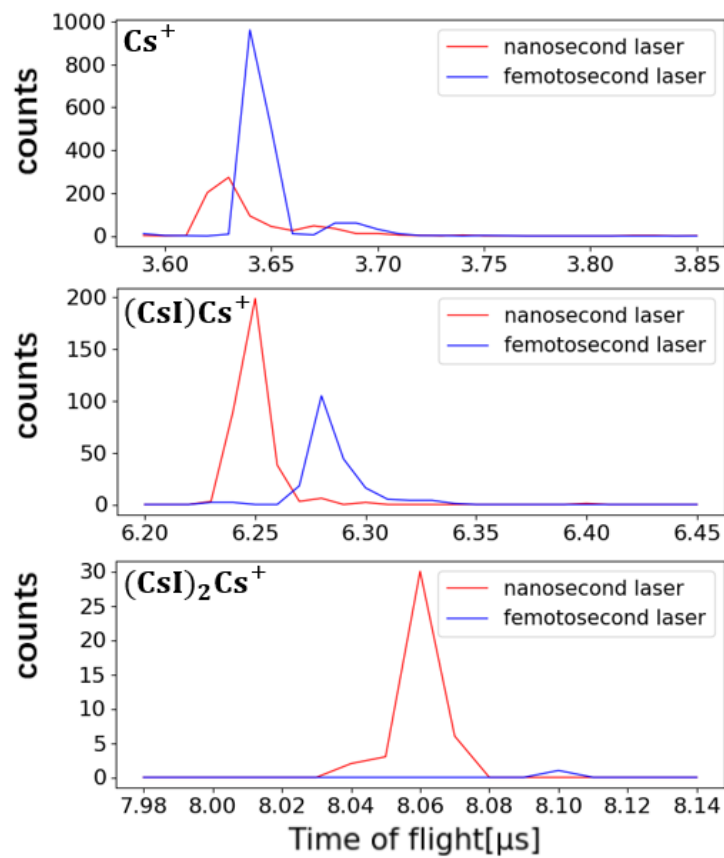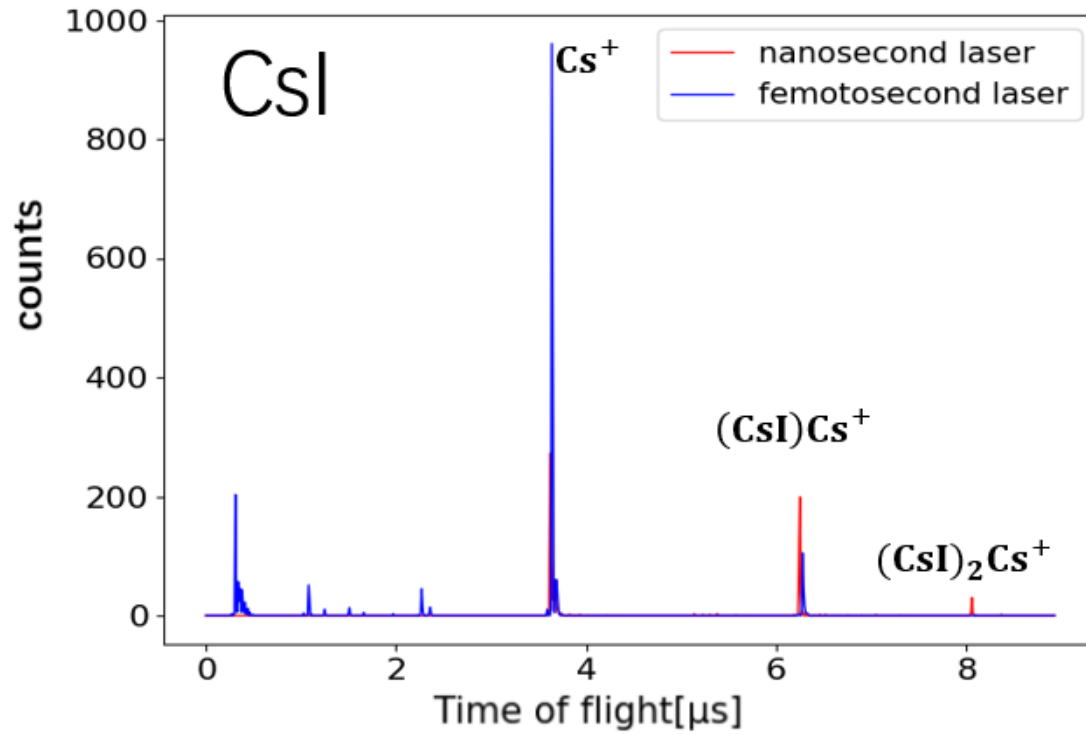
Figure 4.7

The TOF spectra of Cs^+ under femtosecond and nanosecond laser are singled out and compared separately with simulation results. As **Figure 4.6** shows, the signal width fits better with the nanosecond laser, but there are differences between the signal peak of the simulated and experimental results. Femtosecond laser better fits the signal width and peak with simulation results.
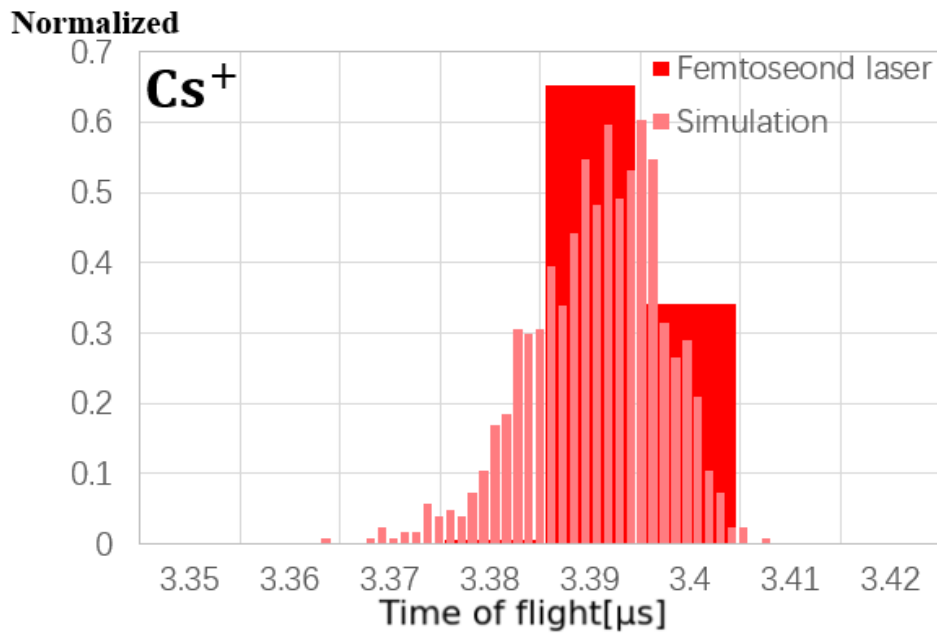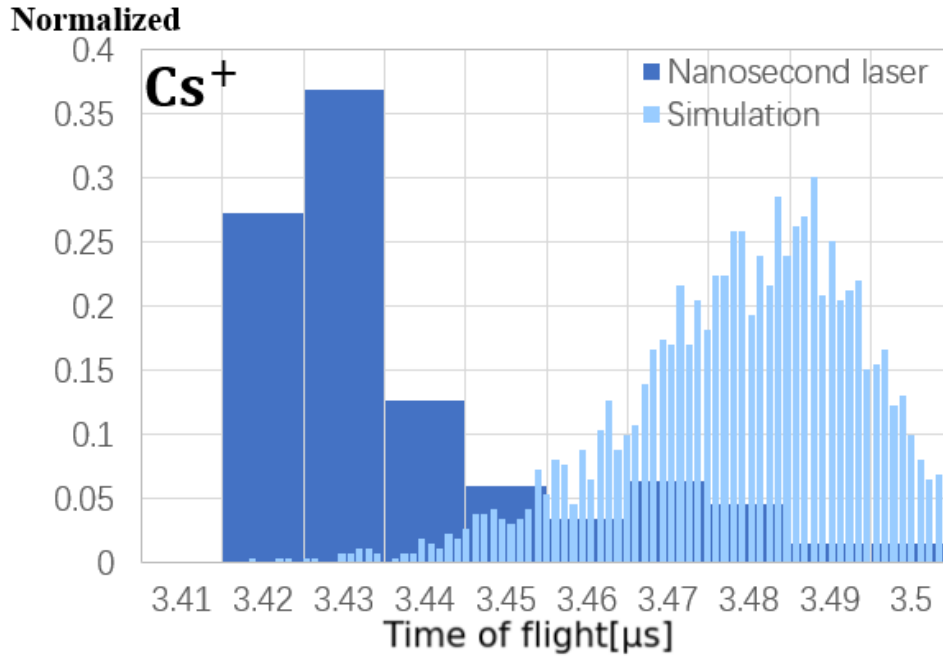

Figure 4.8

4.3 Femtosecond laser intensity dependence of initial velocity distribution

As aforementioned low-intensity femtosecond laser desorption/ionization process prediction, and to expect to desorb and ionize with fast emission in a small number of samples. Therefore, to further figure out the relationship between femtosecond laser intensity and ion initial velocity and temperature. In this section, by controlling the femtosecond laser intensity to observe the actual desorption/ionization process, and the ion temperature and velocity $v_{shifted}$ trend according to the ion TOF spectra. The parameters of the femtosecond laser are shown in Table 4.2.5.

Table 4.2.5.

Sample	CsI
Pulse duration	160 fs
Laser frequency	10 kHz
Pulse energy	1.5/1.0/0.7/0.5μJ

The Cs^+ TOF spectra obtained under the above experimental conditions with different pulse energies are shown in **Figure 4.9.**
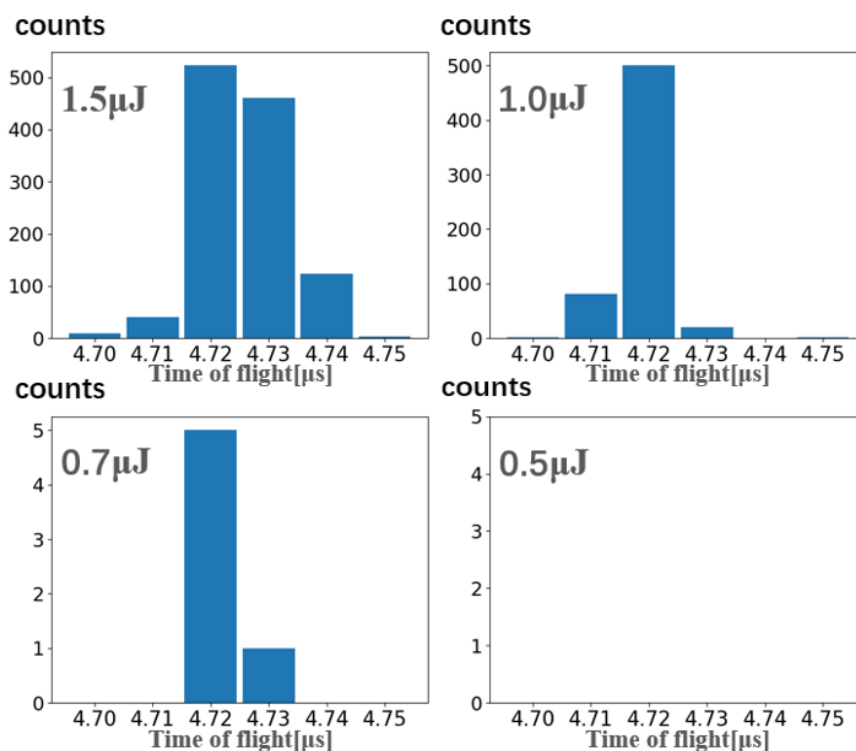
Figure 4.9

71

As shown in the **Figure 4.9.,** with the laser intensity gradually decreases, the count number and τ_{signal} also decrease. When the pulse energy reduces from 1µJ to 0.7 µJ per pulse, the peak count directly from almost 500 decreases to 5, and the signal disappears after the pulse energy keep on decreasing to 0.5 µJ. Therefore, the threshold can be estimated between 0.7 µJ and 0.5 µJ. By recoding signal width of Cs^+ in different pulse energy, and compiled in Table 4.2.6.

Table 4.2.6.

Pulse energy[µJ]	1.5	1.0	0.7	0.5
τ_{signal}[µs]	0.05	0.04	0.03	0
$T[K]$	16000	14000	8000	0
$v_{shifted}$[m/s]	11000	11000	11000	0

The corresponding ion temperature and $v_{shifted}$ at different laser pulse energy based on the signal width can be observed. According to the temperature and $v_{shifted}$ results, it can be seen that as the laser pulse energy decreases, the temperature of the ions decreases gradually, but the ion $v_{shifted}$ remains unchanged.

5 Summary

We developed a time-of-flight (TOF) mass spectrometer using the ultrashort laser pulse as a desorption/ionization source, combining with ion trajectory simulations and the signal analysis which enabled us to determine the initial velocity distribution of the emitted ions.

For the simulation of ion trajectories in the electric acceleration field of the TOF mass spectrometer, the potential simulation code using the relaxation method, Bessel function method, and the surface charge method were examined and compared. The surface charge method was chosen for trajectory simulation because of its flexibility and high calculation speed.

The laser-induced ion initial velocity distribution based on the shifted Maxwell–Boltzmann model was employed, and combined with trajectory simulation the ion TOF spectra was analyzed.

We have shown that the three different positive ions of the mixed sample of CsI, KI, and NaI under different femtosecond laser intensity. By increasing the femtosecond laser intensity to higher, the three species ions temperature also increases but $v_{shifted}$ term remains stable. For the nanosecond laser and femtosecond laser comparison research, the laser induced formation of CsI ion cluster was observed for femtosecond and nanosecond lasers with the same pulse energy of 2.5 μJ per pulse, and the estimation of ion temperature and $v_{shifted}$ of laser desorption/ionization of cesium iodide clusters were presented. In nanosecond laser case, it is shown that the $(CsI)_n Cs^+ (n = 0,1,2)$ clusters yield was observed, but in femtosecond laser case $(CsI)_2 Cs^+$ was not observed. In the femtosecond laser intensity dependence experiment with sample CsI, as the laser pulse energy decreased, the estimated temperature of Cs^+ also decreased, but the ion $v_{shifted}$ remains unchanged.

6   Acknowledgements

References

[1]   Karas, Michael, and Franz Hillenkamp. "Laser desorption ionization of proteins with molecular masses exceeding 10,000 daltons." *Analytical chemistry* 60.20 (1988): 2299-2301.

[2]   Strickland, Donna, and Gerard Mourou. "Compression of amplified chirped optical pulses." *Optics communications* 55.6 (1985): 447-449.

[3]   Verhoff, B., S. S. Harilal, and A. Hassanein. "Angular emission of ions and mass deposition from femtosecond and nanosecond laser-produced plasmas." *Journal of Applied Physics* 111.12 (2012): 123304.

[4]   Freeman, J. R., et al. "Comparison of optical emission from nanosecond and femtosecond laser produced plasma in atmosphere and vacuum conditions." *Spectrochimica Acta Part B: Atomic Spectroscopy* 87 (2013): 43-50.

[5]   Gamaly, Eugene G., and Andrei V. Rode. "Physics of ultra-short laser interaction with matter: From phonon excitation to ultimate transformations." *Progress in Quantum Electronics* 37.5 (2013): 215-323.

[6]   Stephens, W.E. A Pulsed Mass spectrometer 1946,69,691

[7]   Vestal, M. L., P. Juhasz, and S. A. Martin. "Delayed extraction matrix‐assisted laser desorption time‐of‐flight mass spectrometry." *Rapid Communications in Mass Spectrometry* 9.11 (1995): 1044-1050.

[8]   Mamyrin, B. A. "Time-of-flight mass spectrometry (concepts, achievements, and prospects)." *International Journal of Mass Spectrometry* 206.3 (2001): 251-266.

[9]   Ioanoviciu, Damaschin. "Ion‐Optical solutions in time‐of‐flight mass spectrometry." *Rapid communications in mass spectrometry* 9.11 (1995): 985-997.

[10]   Toyoda, Michisato, et al. "Multi‐turn time‐of‐flight mass spectrometers with electrostatic sectors." *Journal of mass spectrometry* 38.11 (2003): 1125-1142.

[11]   Gattass, Rafael R., and Eric Mazur. "Femtosecond laser micromachining in transparent materials." *Nature photonics* 2.4 (2008): 219-225.

[12]   Rethfeld, B., et al. "Timescales in the response of materials to femtosecond laser excitation." *Applied Physics A* 79 (2004): 767-769.

[13]   Gamaly, Eugene G., and Andrei V. Rode. "Physics of ultra-short laser interaction with matter: From phonon excitation to ultimate transformations." *Progress in Quantum Electronics* 37.5 (2013): 215-323.

[14]   Harilal, Sivanandan S., et al. "Femtosecond laser ablation: Fundamentals and applications." *Laser-Induced Breakdown Spectroscopy: Theory and Applications* (2014): 143-166.

[15]   Kools, J. C. S., et al. "Gas flow dynamics in laser ablation deposition." *Journal of Applied Physics* 71.9 (1992): 4547-4556.

[16]   Ye, Mengqi, and Costas P. Grigoropoulos. "Time-of-flight and emission spectroscopy study of femtosecond laser ablation of titanium." *Journal of Applied Physics* 89.9 (2001): 5183-5190.

[17]   Torrisi, L., et al. "Tantalum ions produced by 1064 nm pulsed laser irradiation." *Journal of applied physics* 91.7 (2002): 4685-4692.

[18]   Apinaniz, Jon I., et al. "Ion kinetic energy distributions and mechanisms of pulsed laser ablation on Al." *The Journal of Physical Chemistry C* 112.42 (2008): 16556-16560.

[20]   Operator's Manual Verdi^{TM} 8/10Diode-Pumped Lasers

[21]   Operator's Manual The Coherent Mira Optimal 900-F Laser

[22]   Operator's Manual Rega Model 9000 Laser

[23]   Aoki, J., et al. "Simulation of ion trajectories using the surface-charge method on a special purpose computer." *Nuclear Instruments and Methods in Physics Research Section A: Accelerators, Spectrometers, Detectors and Associated Equipment* 600.2 (2009): 466-470.

[24]   宅間董「数値電界計算の基礎と応用（理工学講座）」

[25]   Heddle, Douglas WO. *Electrostatic lens systems*. CRC Press, 2000.

[26]   Heddle, D. W. O. "Accurate calculation of cylinder lens potentials using the nine-point relaxation and Bessel expansion methods." *Journal of Physics D: Applied Physics* 32.13 (1999): 1447.

[27]   Chang, Zenghu. *Fundamentals of attosecond optics*. CRC press, 2016.

[28]   https://refractiveindex.info/?shelf=glass&book=SF11&page=SCHOTT

[29]   Fernández-Lima, F., et al. "Laser ablation of CsI analyzed by delayed extraction." *Applied surface science* 217.1-4 (2003): 202-209.

[30]   Collado, V. M., et al. "Laser induced formation of CsI ion clusters analyzed by delayed extraction time-of-flight mass spectrometry." *Physical Chemistry Chemical Physics* 7.9 (2005): 1971-1976.